atmosphere

MDPI

*Article*

# Atmospheric Processes over the Broader Mediterranean Region: Effect of the El Niño–Southern Oscillation?

**Harry D. Kambezidis** [1,2]

[1] Emeritus Researcher, Atmospheric Research Team, Institute of Environmental Research and Sustainable Development, National Observatory of Athens, GR-11810 Athens, Greece; harry@noa.gr
[2] Research Associate, Laboratory of Soft Energies and Environmental Protection, Department of Mechanical Engineering, University of West Attica, GR-12241 Athens, Greece

**Featured Application: Various studies have reported a teleconnection between the El Niño phenomenon in the southern Pacific Ocean and the North-Atlantic Oscillation, which governs the weather in the eastern side of the American continent and most parts of Europe, including the Mediterranean. Though such a relationship has been established to a large degree, it is still unknown whether the El Niño phenomenon can affect atmospheric processes in the mentioned regions. Therefore, the present study investigates the existence of any effect of El Niño on atmospheric radiation and atmospheric aerosols over the Mediterranean region.**

**Abstract:** The Mediterranean area is considered a hot spot on our planet because it represents the crossroads of various aerosols. Several studies have shown that the weather in the region is affected by the North-Atlantic Oscillation, which, in turn, is well connected with the El Niño–Southern Oscillation (ENSO) phenomenon. Nevertheless, no study has investigated the ENSO effect on the solar radiation and atmospheric aerosols in this region. The present study considers a greater area around the Mediterranean Sea over the period 1980–2022. The results show that there exists a loose but significant dependence, in some cases, of the optical properties of aerosols (aerosol optical depth, Ångström exponent, cloud optical depth) and solar radiation (net short-wave and net long-wave radiation, direct aerosol radiative forcing) on ENSO events. The results of this study provide motivation for further investigations, since such results can increase the accuracy of general circulation models that deal with climate change. Besides the ENSO effect, the enrichment of the Mediterranean atmosphere in suspended particles from great volcanic eruptions is shown. The inter-annual variation of the examined parameters is presented. A classification of the existing aerosols over the area is also provided.

**Keywords:** atmospheric radiation; atmospheric aerosols; North-Atlantic Oscillation; El Niño–Southern Oscillation; Mediterranean region

check for updates

**Citation:** Kambezidis, H.D. Atmospheric Processes over the Broader Mediterranean Region: Effect of the El Niño–Southern Oscillation? *Atmosphere* **2024**, *15*, 268. https://doi.org/10.3390/atmos15030268

Academic Editor: Sunling Gong

Received: 17 January 2024
Revised: 12 February 2024
Accepted: 20 February 2024
Published: 23 February 2024

**Copyright:** © 2024 by the author. Licensee MDPI, Basel, Switzerland. This article is an open access article distributed under the terms and conditions of the Creative Commons Attribution (CC BY) license (https://creativecommons.org/licenses/by/4.0/).

## 1. Introduction

Atmospheric radiation refers to the flow of electromagnetic energy from the Sun to the Earth's surface; it is influenced by clouds, aerosols, and gases in the atmosphere [1]. Atmospheric aerosols are solid or liquid particles suspended in the air. They play an important role in the Earth's energy budget [2,3] and the Earth's climate system [4] by scattering and absorbing solar radiation [5]. They also play a significant role in global climate change by contributing to the warming or the cooling effect, depending on their concentration, chemical composition, size, and altitude in the atmosphere [6]. Some particles in the atmosphere can be considered primary aerosols (dust, sea salt, black carbon, volcanic debris), while others may come from chemical reactions (including sulphates, nitrates, ammonium, and secondary organic compounds). Therefore, atmospheric aerosols are of natural or anthropogenic origin or a mixture of both. Purely scattering aerosols include sulphates,

nitrates, ammonium, and sea-salt particles; absorbing aerosols are primarily black carbon, with dust and organic carbon having partly absorbing and partly scattering properties in the ultra-violet spectrum [7]. Atmospheric aerosols show direct and indirect effects; the first category includes their scattering and absorption properties, and the second comprises their ability to act as cloud condensation nuclei [8]. Although the atmospheric aerosols' optical properties are well known, there are still large uncertainties associated with their climate implications due to the large variety of types, their always-changing optical and physicochemical properties, their influence on meteorology (weather modification), and their mixing processes in the atmosphere [9]. Atmospheric aerosols interact with solar radiation through the scattering and absorption mechanisms in the atmosphere; therefore, an increased/decreased aerosol concentration can affect (decrease/increase) solar radiation, a phenomenon that can be maximised under clear skies. Because of the above, atmospheric aerosols are a large source of uncertainty in climate projections [10], and precise information on these aerosols must be known if accurate estimates of the solar energy availability at a location are sought [11].

The attenuation of solar radiation due to atmospheric aerosols is generally called atmospheric turbidity, which refers to the clearness (transparency) of the atmosphere in terms of the degree of solar radiation extinction [12]. Atmospheric science (or atmospheric radiation) has quantified this effect by defining various factors: (i) the Linke turbidity factor expresses the number of ideal (hypothetical) clean-dry atmospheres to produce the observed attenuation of the extraterrestrial radiation by the real atmosphere under clear skies [13]; (ii) the Unsworth–Monteith turbidity coefficient expresses the absorption of solar light by a dust-laden atmosphere relative to a dust-free one, when both atmospheres have a specific amount of water-vapour content [14]. In this context, some other solar radiation ratios have been proposed to describe its attenuation through the atmosphere: (i) the clearness index is the global solar radiation value needed to make up for the extraterrestrial radiation [15]; (ii) the diffuse fraction expresses the diffuse solar radiation value needed to make up for the global solar radiation value [16]. Recently Kambezidis et al. [17] used this index to classify skies into clear, intermediate, and overcast.

There are various large-scale atmospheric/oceanic circulation phenomena on Earth that influence the weather not only around the immediate territory but at longer distances as well. These are the El Niño–Southern Oscillation (ENSO), the North-Atlantic Oscillation (NAO), the Northern Annular Mode (NAM), the North-Pacific Oscillation (NPO), the Pacific–North American Pattern (PNA), the Hadley, Ferrel, and Polar Cells, the Rossby Waves, the Arctic and Quasi-Biennial Oscillations (AO, QBO), the Pacific Decadal Oscillation (PDO), and the Atlantic Multi-Decadal Oscillation (AMO). The most known and studied of them are the ENSO and NAO. Yoo et al. [18] examined the significance of the AO, ENSO, and NAO circulations and agreed with [19] that recent ENSO activities are important because the variability of NAO is anticipated to be more dependent on ENSO in the future [19]. Abish and Mohanakumar [20] showed that the El Niño years exhibit a significant increase in aerosol concentration over the Indian sub-continent, a fact that is evident from high aerosol-index values. Laken and Stordal [21] analysed the HBGWL (Hess Brezowsky Großwetterlagen) European weather data and found that the European weather shows a clear and significant response to the peak NAO phases (both positive and negative); on the contrary, they were not able to find any robust relationship in European weather related to the peaks in the solar cycle and/or ENSO. Kirov and Georgieva [22], on the other hand, found a close relationship between the NAO and ENSO circulations and solar activity. Mezzina et al. [23] highlighted that the ENSO phenomenon has been shown to contribute to the north Atlantic mid-latitude weather predictability at the surface. Casselman et al. [24,25] also confirmed the teleconnection between the ENSO and NAO circulation modes in coupled climatic models. García-Serrano et al. [26] revisited the timing of the ENSO–Tropical North Atlantic relationship. Liu et al. [27] reported that there exists a strong positive teleconnection between the ENSO phenomenon in the winter and the tropospheric carbon-oxide levels over the North-Atlantic European region in the follow-

ing spring (March to May). Alpert et al. [28] corroborate that the South Asian Monsoon plays a significant role in influencing the climate of the central and eastern Mediterranean. Mariotti et al. [29] showed that the inter-annual precipitation variability over the Euro-Mediterranean region is significantly influenced by the El Niño phenomenon, as dependent on the season. In a more detailed study, Mathbout et al. [30] demonstrate the major role of the Western Mediterranean Oscillation (WeMO) and the Mediterranean Oscillation in modulating precipitation over the north-western Mediterranean, while high daily rainfalls over south France, northeast Spain, Croatia, and Tunisia are linked to low WeMO values and high East-Atlantic Oscillation ones. In a study from the 1980s, Ropelewski and Halpert [31] found a close relationship between the El Niño phases and the precipitation patterns over Australia, the Americas, the Indian sub-continent, and Africa. On the other hand, Urdiales-Flores et al. [32] showed that the Mediterranean Basin bas been warming, over the last 120 years (1901–2020), more rapidly than the global rate; they attributed this warming amplification to the combined effect of reduced aerosol loading and a decrease in soil moisture over the region. Chiacchio and Wild [33] attributed the all-sky solar radiation changes over Europe in the period 1970–2000 to the NAO and more specifically to the cloud-cover variability associated with the NAO phases; they also indicated the role of aerosols in this process.

Though the teleconnection between the ENSO and NAO circulations has been established as shown above, it is questionable whether ENSO may have an influence on the atmospheric processes over the Mediterranean (namely, atmospheric radiation and atmospheric aerosols). To the best of the author's knowledge, no such study has been conducted thus far. Nevertheless, little research has demonstrated the impact of the ENSO phenomenon on aerosol particles in the broader vicinity of the event. Westervelt et al. [34], based on coupled chemistry–climate models, concluded that regional aerosol emission reductions tend to cause a shift to the positive ENSO phase (El Niño). Huang et al. [35] found that the ENSO-related sea-surface temperature anomalies in the tropical eastern Pacific have a significant effect on the suspended dust particles in the region from the Arabian Peninsula to central Asia. Banerjee and Kumar [36] showed that the El Niño can modulate the strength of dust subsidence over the Indian sub-continent by remotely changing the strength of convection over the India-Pacific region. The Mediterranean region is considered by many researchers to be a hot spot in terms of aerosol events from various sources (air pollution from large cities or industrial areas [37,38], transport of dust from the Sahara Desert [39–43], and the effects of volcano eruptions [44,45] and wildfires [46]). Figure 1 of [47] is very informative as far as the Sahara dust and air-pollutant transport over the Mediterranean area is concerned.

The parameters examined in this study as atmospheric processes are the net solar radiation levels (netSW, netLW) over the Mediterranean and the corresponding DARF, in addition to the optical and physical characteristics of the local aerosols ($AOD_{550}$, COD, $AE_{470–870}$), as well as any variations in the ground albedo ($\rho_g$). The purpose of the present study is to show whether a relationship between $ONI_{3.4}$ (a measure of the ENSO phenomenon) and the above parameters exists. Such an attempt has not been made in the international literature thus far. Conversely, a strong correlation has been established between the El Niño/La Niña phenomena in the southern Pacific Ocean and its impact on global weather patterns (such as monsoons, e.g., [48–50], in the north Atlantic Ocean near the east coast of the United States and western Europe, e.g., [51,52]). Hazy evidence of a direct ENSO influence on the Mediterranean climate, e.g., [53], exists. Therefore, the emerging issue is how ENSO impacts the atmospheric dynamics over the Mediterranean region, which, in turn, influences atmospheric aerosols.

From the above, the present study forms the hypothesis that the ENSO circulation may have an effect on the atmospheric processes over the wider Mediterranean area. This hypothesis is based on the following remarks: (i) there is an established teleconnection between the ENSO phenomenon and the weather modification over the wider north Atlantic area; (ii) atmospheric aerosols are affected by weather patterns (rain and wind

for washout and transport, respectively) and, therefore, by the NAO phases [54]; and (iii) the extent of such weather patterns over the Mediterranean area may also affect the atmospheric processes. Therefore, the present study seeks to find the degree of the ENSO effect on the Mediterranean aerosols.

The work is divided into sections. Section 1 provides the current state of knowledge on the subject. Section 2 provides the data and the methodology used in this work. Section 3 presents the results of the study. Section 4 provides a discussion of the results, how they can be interpreted from the perspective of previous studies, and how the working hypothesis is proven to be sound. Section 5 provides the main findings of this work. Finally, Appendix A, acknowledgements, and references are presented.

## 2. Materials and Methods

The following parameters are examined in this work in the sense of atmospheric processes: net short-wave and net long-wave radiation, clouds (cloud optical depth), and atmospheric optical properties (aerosol optical depth, Ångström exponent). Additionally included are the ground albedo, the indices for the North-Atlantic Oscillation (NAO) and the El Niño–Southern Oscillation (ENSO), and the sunspot number (SSN).

The Giovanni platform, which can be accessed for free at https://giovanni.gsfc.nasa.gov/giovanni (accessed on 18 October 2023) [55], provided monthly data for the years 1980–2022 (43 years or 4.3 decades) at a spatial resolution of 0.5° × 0.625°, which covers the broader Mediterranean region (longitudes 6° W–35° E, latitudes 30° N–45° N). The following data were downloaded: net short-wave (netSW) radiation at the bottom-of-the-atmosphere (BOA) with and without aerosols in the atmosphere ($netSW_{BOA,A}$ and $netSW_{BOA,NA}$, respectively, in $Wm^{-2}$; MERRA-2 model; Giovanni files M2TMNXRAD v5.12.4); netSW radiation at the top-of-the-atmosphere (TOA) with and without aerosols in the atmosphere ($netSW_{TOA,A}$ and $netSW_{TOA,NA}$, respectively, in $Wm^{-2}$; MERRA-2 model; Giovanni files M2TMNXRAD v5.12.4); net long-wave (netLW) radiation at the surface with and without aerosols in the atmosphere ($netLW_{BOA,A}$ and $netLW_{BOA,NA}$, respectively, in $Wm^{-2}$; MERRA-2 model; Giovanni files M2TMNXRAD v5.12.4); netLW radiation at the TOA with and without aerosols in the atmosphere ($netLW_{TOA,A}$ and $netLW_{TOA,NA}$, respectively, in $Wm^{-2}$; MERRA-2 model; Giovanni files M2TMNXRAD v5.12.4); surface albedo ($\rho_g$; spatial resolution of 0.25°; GLDAS model; Giovanni files GLDAS NOAH025 Mv2.0 and GLDAS NOAH025 Mv2.1); scattering aerosol optical depth at 550 nm ($SAOD_{550}$; MERRA-2 model; Giovanni file M2TMNXAER v5.12.4); dust aerosol optical depth at 550 nm ($DAOD_{550}$; MERRA-2 model; Giovanni file M2TMNXAER v5.12.4); total aerosol optical depth at 550 nm ($TAOD_{550}$; MERRA-2 model; Giovanni file M2TMNXAER v5.12.4); cloud optical depth (COD; MERRA-2 model; Giovanni file M2TMNXRAD_v5.12.4); and Ångström exponent in the spectral band 470–870 nm ($AE_{470-870}$; MERRA-2 model; Giovanni file M2TMNXAER v5.12.4). Furthermore, monthly mean data for the following parameters were downloaded between 1980 and 2022: (i) the sunspot number (SSN) from the WDC-SILSO, Royal Observatory of Belgium (data available free of charge at: https://www.sidc.be/SILSO/datafiles (accessed on 18 October 2023)); (ii) the North-Atlantic Oscillation Index (NAOI) from the National Centres for Environmental Information, National Oceanic and Atmospheric Administration (NOAA), USA (data available free of charge at: https://www.cpc.ncep.noaa.gov/products/precip/CWlink/pna/norm.nao.monthly.b5001.current.ascii.table (accessed on 19 October 2023)); and (iii) the Oceanic El Niño Index 3.4 ($ONI_{3.4}$) from the Climate Prediction Centre, National Weather Service, NOAA, USA (data available free of charge at: https://origin.cpc.ncep.noaa.gov/products/analysis_monitoring/ensostuff/ONI_v5.php (accessed on 18 October 2023)). The selected domain for this work, encompassing the broader Mediterranean region, is depicted in Figure 1.




**Figure 1.** The domain around the Mediterranean region covered in this study. The lower left corner of the rectangle has geographical coordinates (6° W, 30° N), and the upper right one (35° E, 45° N).

The direct aerosol radiative forcing (DARF) in the atmosphere was estimated using netSW and netLW data. Clear-sky (CS) conditions have been considered throughout this study. The expressions for the net radiations are the following [1]:

$$\mathrm{DARF} = (Q_A - Q_{NA})_{TOA} - (Q_A - Q_{NA})_{BOA}, \quad (1)$$

$$Q_A = \mathrm{netSW}_A - \mathrm{netLW}_A, \quad (2)$$

$$Q_{NA} = \mathrm{netSW}_{NA} - \mathrm{netLW}_{NA}, \quad (3)$$

$$\text{either netSW or netLW} = F\downarrow - F\uparrow. \quad (4)$$

In the above equations, Q symbolises the difference between netSW and netLW, while either netSW or netLW is the difference between the downward (F↓) minus the upward (F↑) radiation flux (by convention, downward fluxes are positive, upward ones negative). The subscripts A and NA indicate, respectively, an atmosphere with and without aerosols. The Mediterranean region, depicted in Figure 1, is treated as a single entity; that is, all parameter values are time series of monthly data averaged over the chosen domain in the Mediterranean in the period 1980–2022.

The albedo of a surface ($\rho_g$) is defined [1] as the ratio of the reflected SW radiation from a surface to the incident global solar irradiance on it:

$$\rho_g = H_r / H_g, \quad (5)$$

where $H_g$ and $H_r$ are the global solar irradiance on the surface and the reflected radiation from it, respectively. The monthly mean values of $\rho_g$ were obtained from the Giovanni platform by matching two distinct time series for the years 1948–2014 (NOAH025 Mv2.0 file) and 2000–2022 (NOAH025 Mv2.1 file) and having an overlapping period (2000–2014). To overcome this problem and unify both time series in the period 1948–2022, the following averaging methodology was implemented. The $\rho_g$ values in the common period 2000–2014 were computed as a weighting function on the concurrent values:

$$\rho_{g2000–2014} = 0.5 \cdot \rho_{g(\text{for only 2000–2014 during 1948–2014})} + 0.5 \cdot \rho_{g(\text{for only 2000–2014 during 2000–2022})}, \quad (6)$$

which implies an equal influence of the older and newer time series on the result. The choice of the weighting factor of 0.5 was based on the rationale that the difference (gap) between the two $\rho_g$ time series in the year 2000 is not high (just +0.0038 or +1.7%); since there is no published evaluation of the accuracy of these two satellite-derived time series in the literature, to the knowledge of the author, it would, therefore, be wise to reduce their

difference to half. This means that the $\rho_{g2000–2014}$ values in the 1948–2014 time series were increased by 0.0038, while the values in the 2000–2022 time series were reduced by 0.0038. Figure 2 depicts this process of matching. The variations in $\rho_g$ were caused by several meteorological phenomena that occurred over the selected area of the Mediterranean between 1980 and 2022. These include snowfall in the winter, at least in the European portion of the domain, variations in cloud cover, and variability in the aerosol loading; these may have had an impact on the region's satellite-observed atmospheric albedo.

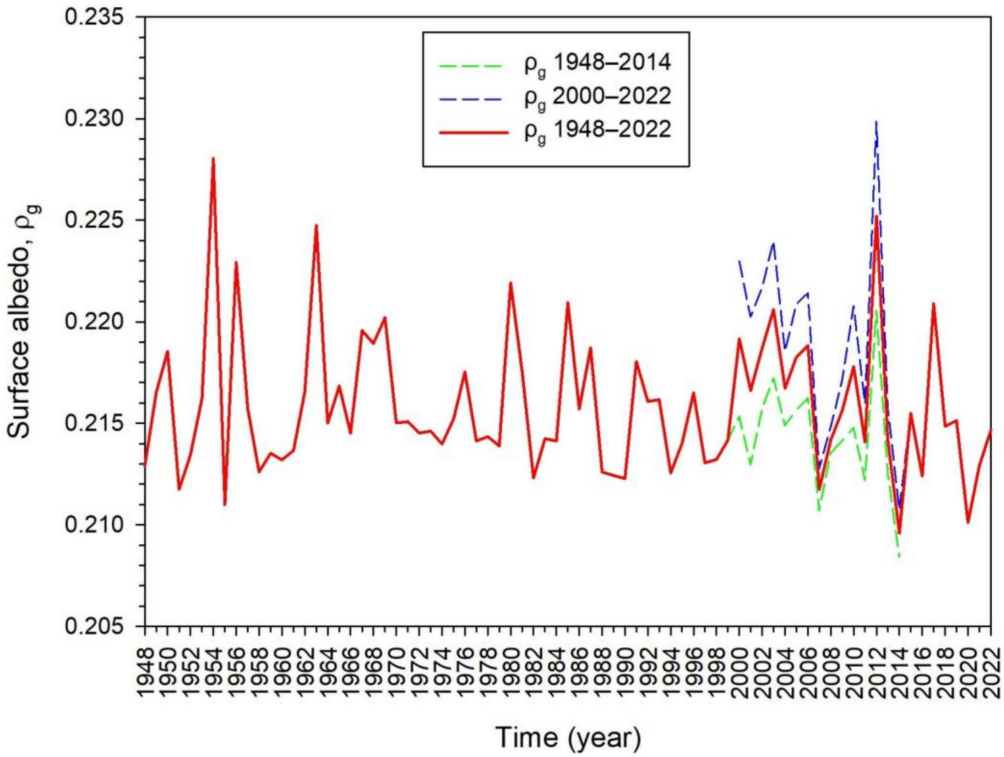



**Figure 2.** The three surface-albedo ($\rho_g$) time series over the Mediterranean region in the periods 1948–2014 (v2.0), 2000–2022 (v2.1), and 1948–2022 (concatenated v2.0 and 2.1). The annual $\rho_g$ values are spatial averages over the entire domain shown in Figure 1.

The absorption and scattering aerosol optical depths at the wavelength of 550 nm are given by the following equations [56]:

$$TAOD_{550} = \tau_{t,550} - \tau_{r,550} - \tau_{wv,550} - \tau_{O3,550} - \tau_{mg,550}, \quad (7)$$

$$TAOD_{550} = SAOD_{550} + AAOD_{550}. \quad (8)$$

In the above equations, $\tau$ is the optical depth due to a specific process in the atmosphere (subscripts t for the total extinction of solar radiation in the Earth's atmosphere, r for Rayleigh scattering, wv for water-vapour attenuation, $O_3$ for ozone, and mg for mixed gases); TAOD is the total extinction coefficient of the solar radiation due to aerosols, which is the sum of the aerosol scattering and absorption extinction coefficients, SAOD and AAOD, respectively. Taking the difference between the $TAOD_{550}$ and $SAOD_{550}$ values from Equation (8), the $AAOD_{550}$ values were calculated.

El Niño (warm) and La Niña (cool) episodes in the eastern Pacific Ocean are classified using the $ONI_{3.4}$ standard by NOAA (https://origin.cpc.ncep.noaa.gov/products/analysis_monitoring/ensostuff/ONI_v5.php (accessed on 18 October 2023)). This is an index [57] for tracking the oceanic part of the ENSO climatic pattern. It is computed as a running 3-month mean sea-surface temperature (SST) anomaly for the El Niño region (5° S–5° N, 120° W–170° W). An event is categorised as warm if the SST anomaly for

5 consecutive overlapping 3-month periods is $\geq$+0.5 °C; if it is $\leq$−0.5 °C, it is classified as cool. In the rest of the article, $ONI_{3.4}$ will be referred to as ONI.

The NAOI is based on the surface sea-level pressure difference between the subtropical High at Azores and the sub-polar Low over Iceland. Positive values of the NAO index (NAOI) indicate below-normal pressures across the high latitudes of the North Atlantic and above-normal pressures over the central part of the North Atlantic Ocean, the eastern United States, and western Europe [58]. Negative NAOI values reflect opposite pressure anomalies over these regions [58]. The NAO phenomenon is strictly associated with the Gulf Stream, which originates in the Gulf of Mexico and travels northward along the Atlantic. High positive NAOI phases are linked to above-normal temperatures in the eastern United States and across northern Europe and below-normal temperatures in Greenland and often across southern Europe and the Middle East. They deliver above-normal precipitation over northern Europe and Scandinavia and below-normal precipitation patterns over southern and central Europe [59]. Severe adverse (negative) NAOI phases are associated with opposite temperature and precipitation patterns than those observed during strong positive NAO events. The method for calculating NAOI is described in [60]. It should be mentioned here that there are different NAOI definitions, since other station-based indices and principal component-based indices exist.

COD is a fundamental cloud property that determines the Earth's energy budget [61]. It is derived from satellite or ground-based observations, e.g., [61–63].

AE is the exponent in the Ångström wavelength-dependent formula for describing the extinction of solar light by atmospheric aerosols ($\tau_a$ ($\lambda$)). The Ångström formula is [1]:

$$\tau_a(\lambda) = \beta \cdot \lambda^{-AE} \quad (9)$$

where β is the Ångström coefficient or the AOD at the wavelength λ = 1000 nm. The Ångström exponent has been considered in the visible (VIS) wavelength range, i.e., 470–870 nm, in this work. The Ångström coefficient is a measure of the aerosol concentration, while the Ångström exponent indicates size. A usual value of AE = 1.3 is considered; above this threshold, the aerosols are of the fine mode, and below this value the aerosol particles are characterised as coarse.

The sunspot number is associated with the 11-year solar activity. Number 25 is the current solar cycle, which began in December 2019 and is still running. The examined period of 1980–2022 includes solar cycles 22–25.

All correlation coefficients reported in the present work make use of Pearson's formula. To summarise the variables investigated in this work, Table 1 presents a list of the factors used in this study along with pertinent commentary. It is emphasised here that this list includes parameters other than those concerning aerosol properties and large-scale circulation modes, i.e., solar fluxes and cloud properties. This is done in order to investigate the dependence of those factors on NAO and ENSO, because they are strictly related to the aerosol properties.

**Table 1.** List of the parameters used in the present, work with a short description. A = aerosols in the atmosphere, BOA = bottom-of-atmosphere, CS = clear skies, NA = no aerosols in the atmosphere, TOA = top-of-atmosphere.

| Parameter | Remarks | Period | Source |
|---|---|---|---|
| NAOI | North-Atlantic Oscillation index | 1980–2022 | CPC/NCEP/NOAA, USA |
| ONI | Oceanic El Niño index | 1980–2022 | CPC/NCEP/NOAA, USA |
| SSN | Sunspot number | 1980–2022 | WDC/SILSO, Belgium |
| $TAOD_{550}$ | Total aerosol optical depth at 550 nm | 1980–2022 | Giovanni/GSFC/NASA, USA |
| $SAOD_{550}$ | Scattering aerosol optical depth at 550 nm | 1980–2022 | Giovanni/GSFC/NASA, USA |
| $DAOD_{550}$ | Dust aerosol optical depth at 550 nm | 1980–2022 | Giovanni/GSFC/NASA, USA |
| $AAOD_{550}$ | Absorbing aerosol optical depth at 550 nm | 1980–2022 | Giovanni/GSFC/NASA, USA |
| $AE_{470–870}$ | Ångström exponent in the VIS band 470–870 nm | 1980–2022 | Giovanni/GSFC/NASA, USA |

**Table 1.** *Cont.*

| Parameter | Remarks | Period | Source |
|---|---|---|---|
| DARF | Direct aerosol radiative forcing | 1980–2022 | Estimated |
| COD | Cloud optical depth | 1980–2022 | Giovanni/GSFC/NASA, USA |
| $netSW_{BOA,CS,A}$ | Net SW radiation at BOA under CS and presence of A | 1980–2022 | Giovanni/GSFC/NASA, USA |
| $netSW_{BOA,CS,NA}$ | Net SW radiation at BOA under CS without A | 1980–2022 | Giovanni/GSFC/NASA, USA |
| $netSW_{TOA,CS,A}$ | Net SW radiation at TOA under CS and presence of A | 1980–2022 | Giovanni/GSFC/NASA, USA |
| $netSW_{TOA,CS,NA}$ | Net SW radiation at TOA under CS without A | 1980–2022 | Giovanni/GSFC/NASA, USA |
| $netLW_{BOA,CS,A}$ | Net LW radiation at BOA under CS and presence of A | 1980–2022 | Giovanni/GSFC/NASA, USA |
| $netLW_{BOA,CS,NA}$ | Net LW radiation at BOA under CS without A | 1980–2022 | Giovanni/GSFC/NASA, USA |
| $netLW_{TOA,CS,A}$ | Net LW radiation at TOA under CS and presence of A | 1980–2022 | Giovanni/GSFC/NASA, USA |
| $netLW_{TOA,CS,NA}$ | Net LW radiation at TOA under CS without A | 1980–2022 | Giovanni/GSFC/NASA, USA |
| $\rho_g$ | Ground albedo | 1980–2022 | Giovanni/GSFC/NASA, USA |

## 3. Results

Since ENSO, NAO, and solar activity are the three variables that are the most important in the current effort, it is prudent to first demonstrate any relationships between the three variables. As a result, the analysis begins with a graph that illustrates how NAOI and ONI varied annually throughout the Mediterranean between 1980 and 2022. This is shown in Figure 3. NOAA scientists have determined the (−0.5, +0.5) zone as neutral ENSO occurrences; further, they have defined warm El Niño events for ONI ≥ +0.5 and cold La Niña ones for ONI ≤ −0.5 (see https://origin.cpc.ncep.noaa.gov/products/analysis_monitoring/ensostuff/ONI_v5.php (accessed on 18 October 2023)).

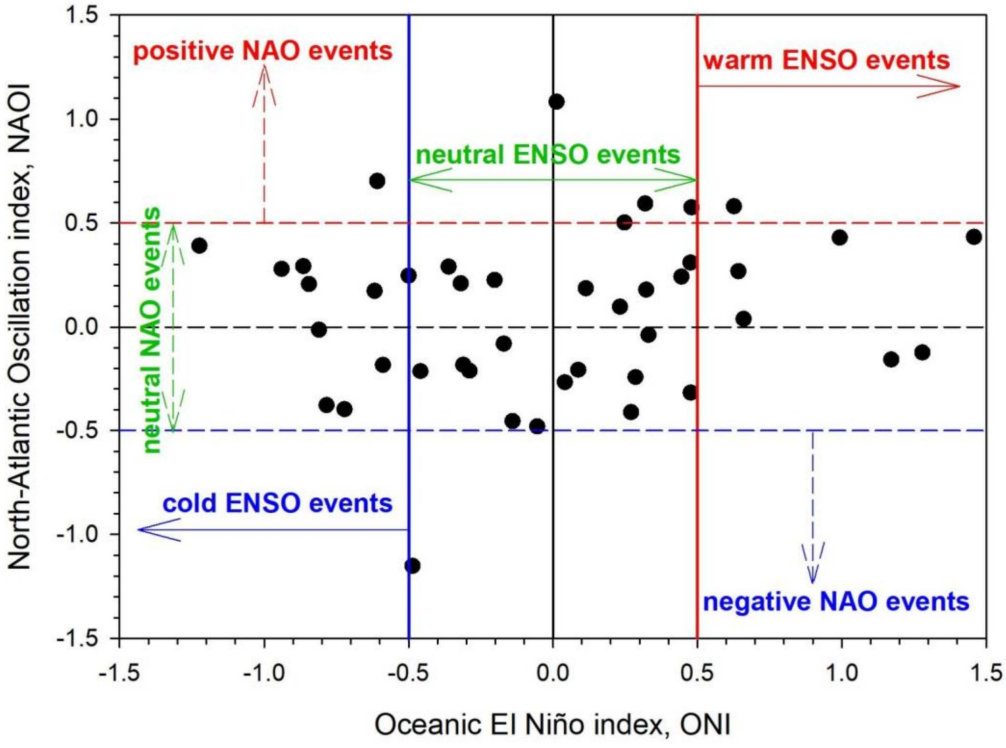



**Figure 3.** Annual mean values of NAOI versus ONI (black dots) over the selected domain in the Mediterranean region in the period 1980–2022. The zone constrained by the blue and red vertical lines indicates neutral ENSO events. ONI values equal to or greater than +0.5 denote (warm) El Niño cases and equal to or less than −0.5 (cold) La Niña events. In this logic, neutral NAO events occur within the boundaries −0.5 < NAOI < +0.5 (blue and red dashed horizontal lines); positive NAOs occur for NAOI ≥ +0.5 and negative for NAOI ≤ −0.5.

As far as the North-Atlantic Oscillation is concerned, a similar neutral zone to that for ONI has not been established. Therefore, it makes sense to use the same delimitation as ONI; that is, neutral NAO events in the band (−0.5, +0.5), positive NAO cases for NAOI ≥ +0.5, and negative NAO events for NAOI ≤ −0.5. According to these definitions, it is evident that many annual occurrences for both ENSO and NAO events fall inside their shared neutral rectangle (see Figure 3), which is created by the intersection of the solid blue/red vertical and dashed blue/red horizontal lines. These data points count 18 values (18 years) out of a total of 43; values on the neutral boundaries count in the adjacent range of values. These dual-neutral years (dual in the sense of concurrent NAOI and ONI neutrality) are (not shown in Figure 3) 1981, 1993, 1995, 1996, 1998, 2001, 2003–2006, 2009, 2012–2014, 2016, 2017, 2019, and 2020. Additionally, in 2010 there was a negative NAO and a nearly neutral ENSO; the years 1989 and 2018 were characterised by positive NAO/almost neutral ENSO and by positive NAO/cold La Niña event, respectively. Moreover, the years 1982, 1987, 1991, 1997, 2002, and 2015 had warm El Niño events and almost neutral NAO; the years 1985, 1988, 1999, 2000, 2007, 2008, 2011, 2021, and 2022 are classified as cold La Niña events and almost neutral NAO. These findings are readily observed in Figure 4, which depicts the evolution of both ENSO and NAO phenomena in the period 1980–2022. The sunspot number (SSN) time series in the same period is added. The NAOI and ONI plots can be shown to be either almost in-phase (as in the years 1982 and 2017) or out-of-phase (as in the years 1988–1990 and 2020–2022). Overall, the correlation coefficient (r) for the NAOI and ONI time series is $r_{NAOI\text{-}ONI} \approx +0.134$ ($p = 0.391 > 0.050$, non-significant at the 95% confidence interval, CI). The SSN time series in Figure 4 shows an almost 11-year cycle; its correlation coefficients with the NAOI and ONI time series are $r_{NAOI\text{-}SSN} \approx +0.211$ ($p = 0.174 > 0.050$, non-significant at the 95% CI), and $r_{ONI\text{-}SSN} \approx +0.021$ ($p = 0.893 > 0.050$, non-significant at the 95% CI). These results can be interpreted as follows.

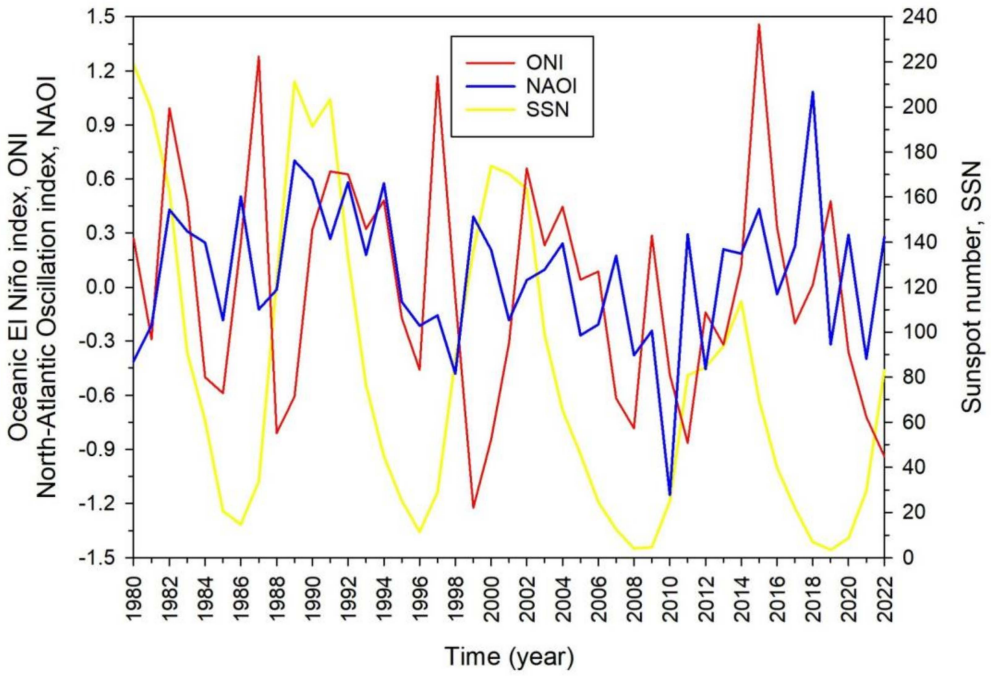



**Figure 4.** Variation of the annual mean ONI, NAOI, and SSN values in the period 1980–2022. Clear low/high ONI values occur 1 year before/after the SSN maximum/minimum. This pattern is not straightforward for NAOI.

1. The correlation is low and positive in all time-series pairs (NAOI-SSN, ONI-SSN, and NAOI-ONI) and non-significant at the 95% CI. Nevertheless, the highest r was found in the case of the NAOI-SSN pair and the least in the ONI-SSN pair.
2. In contrast to the above observation, Kirov and Georgieva [22] studied the influence of the solar activity on NAO and ENSO in the period 1821–1999; they used 30-year

averages of NAOI, ONI, and SSN and found $r_{NAOI\text{-}SSN} = -0.71$, $r_{ONI\text{-}SSN} = -0.76$, and $r_{NAOI\text{-}ONI} = +0.72$, all significant at the 99.99% CI. They, therefore, came to the conclusion that while both ENSO and NAO phenomena control the global climate, their long-term fluctuations are closely linked to solar activity.

3. The discrepancy between Kirov and Georgieva's results and the correlations in the present work may be attributed to the long averaging (filtering) process applied by the former researchers. The present work did not use such a long-term averaging process but only estimation of annual averages from monthly ones.
4. Furthermore, during the period of the present study, NAO decreased/increased with ENSO at low/high levels, during solar maximum/minimum. These observations can be recognised in Figure 4.
5. In more detail, during the 11-year solar cycle, the ENSO phenomenon has a statistically significant minimum of 1 year before the solar maximum, according to [22]. However, this influence is dictated by the strength and location of the centres responsible for these circulation phenomena (pressure differences in the south Pacific and north Atlantic, respectively).
6. Based on the information above, it is unclear whether the ENSO events have a major impact on the NAO circulation; additionally, this seems to ignore ENSO's possible influence on atmospheric radiation and aerosols over the Mediterranean. As a result, the extent of this teleconnection will be examined in the upcoming sections of this paper.

### *3.1. ENSO and Atmospheric Aerosol Properties*

The aerosol characteristics can be described by the total aerosol optical depth at $\lambda$ = 550 nm ($TAOD_{550}$) and the Ångström exponent in the VIS band ($AE_{470–870}$). The first parameter represents the overall attenuation of solar rays by aerosols; it can further be categorised into two values: an absorbing aerosol optical depth ($AAOD_{550}$) and a scattering aerosol optical depth ($SAOD_{550}$), implying absorption and scattering of the solar rays by the presence of aerosols in the atmosphere, respectively (e.g., [64]; also refer to Equation (8)). The Ångström exponent is a measure of the aerosol particle size.

The reliance of TAOD, AAOD, and SAOD on ONI is depicted in Figure 5. $DAOD_{550}$, which is associated with dust-aerosol transport over the Mediterranean region, mainly from the Sahara Desert, is also included; see, e.g., [65]. Low AAOD values in the graph imply low attenuation of solar radiation by absorbing aerosols, a fact that leads to the conclusion of a lower concentration of absorbing aerosols over the Mediterranean in the examined period in comparison to the higher concentration of scattering aerosols (higher SAOD values). Thus, the scattering process is the primary means of reducing solar radiation. This indicates that dispersing aerosols like nitrates, sea salt, and sulphate particles are nearly the only factors reducing solar irradiation across the whole Mediterranean [6]. However, an opposite conclusion was drawn for Greece in the period 2005–2016 by Kambezidis [66] in a study about the solar radiation climate of Greece. This disparity means that to fully understand the aerosol influence throughout the region, the Mediterranean must be studied in smaller areas (portions). Furthermore, as the DAOD values stand between the SAOD and AAOD ones but slightly closer to SAOD, dust aerosols seem to scatter rather than absorb solar radiation (depending on the size of their particles [67]). In fact, in Figure 5, the dust AOD values (dark yellow circles, average $DAOD_{550} \approx 0.089$) fit halfway between the scattering (average $SAOD_{550} \approx 0.202$) and absorption (average $AAOD_{550} \approx 0.011$) processes. Stated differently, the expression $TAOD_{550} = SAOD_{550} + AAOD_{550}$ could instead be rewritten as $TAOD_{550} = (DAOD_{550} + OAOD_{550}) + AAOD_{550}$. This is because, in the event of a Sahara dust outbreak, the scattering particles could include dust particles as well as other particles (such as sea salt, sulphates, and nitrates, denoted as $OAOD_{550}$ in the equation). By replacing the average values of $TAOD_{550} = 0.213$, $SAOD_{550} = 0.202$, $DAOD_{550} = 0.089$, and $AAOD_{550} = 0.011$ in the last expression, it is found that the average $OAOD_{550}$ over the Mediterranean in the period 1980–2022 is 0.100, which is equal to $\approx 9 \cdot AAOD_{550}$. In the same way, $DAOD_{550} \approx 8 \cdot AAOD_{550}$. Therefore, the average

$TAOD_{550} = (9 \cdot AAOD_{550} + 8 \cdot AAOD_{550}) + AAOD_{550} \approx 18 \cdot AAOD_{550}$. This finding indicates that the total solar radiation attenuation in the broader Mediterranean region is 18 times greater than the attenuation resulting from aerosol absorption alone. As a confirmation of the above, Shaheen et al. [68] showed the effect of the meteorological conditions on dust outbreaks over the eastern Mediterranean and Middle East regions; in this context, they linked the DAOD variability over these dust-prone areas to soil moisture, sea-level pressure, air temperature, wind speed, relative humidity, and precipitation.

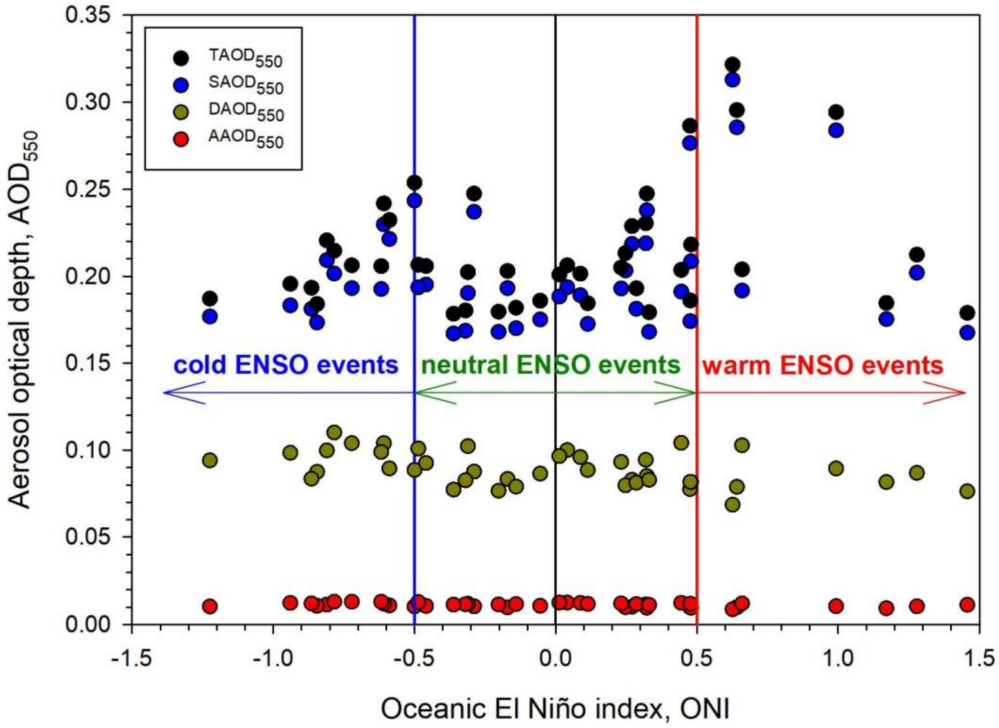



**Figure 5.** Annual mean values of $AOD_{550}$ over the selected domain in the Mediterranean region versus ONI in the period 1980–2022. The zone constrained by the blue and red vertical lines includes neutral ENSO events only. ONI values equal to or greater than +0.5 denote (warm) El Niño cases and equal to or less than −0.5 (cold) La Niña events.

The correlation coefficients between any AOD parameter and ONI are $r_{TAOD550\text{-}ONI} = +0.229$ ($p = 0.140 > 0.050$, non-significant at the 95% CI), $r_{SAOD550\text{-}ONI} = +0.238$ ($p = 0.125 > 0.050$, non-significant at the 95% CI), $r_{AAOD550\text{-}ONI} = -0.431$ ($p = 0.004 < 0.050$, significant at the 99% CI), and $r_{DAOD550\text{-}ONI} = -0.388$ ($p = 0.010 < 0.050$, significant at the 95% CI). These correlations indicate that while $TAOD_{550}$ and $SAOD_{550}$ have a (weak) co-variation with ONI, $AAOD_{550}$ and $DAOD_{550}$ show a (stronger) anti-correlation with ONI. A preference in AOD values in neutral and negative ONI phases is shown in Figure 5, as most ($AOD_{550}$, ONI) data pairs fall in the ONI < +0.5 zone. This is valid, at least, for the years 1980–2022, but more research must be done on this issue.

The average $TAOD_{550}$ over the Mediterranean during the studied period in the present work is 0.213, which is similar to the 0.207 value for the eastern Mediterranean found by Ozdemir et al. [69] for the years 1999–2018. Chiapello et al. [70] discovered that the average $TAOD_{550}$ value for the Mediterranean region between 2005 and 2013 was 0.150 (the average values for the northern, central, and eastern Mediterranean regions were 0.141, 0.143, and 0.167, respectively, as shown in their Table 1b). This value is significantly lower than the value identified in the current study. Kaskaoutis et al. [71], in a study of the aerosol loading over the Athens area in Greece, found a high yearly average of $TAOD_{550} = 0.35$ due to the city's pollution effect on solar radiation (examined period: 2000–2005). Mallet et al. [72] found $AOD_{440}$ values over the Mediterranean region in the period 1996–2012 (mostly within 2003–2012) in the range of 0.15–0.32; these values agree well with the ones found in the present work (0.18–0.32).

Linear regression fits to all four $AOD_{550}$ parameters in the period of the study (not shown in Figure 5) denote increasing trends for $TAOD_{550}$ and $SAOD_{550}$, with values of $+0.0125 \cdot TAOD_{550}$ units per ONI unit ($R^2$ = 0.0524, non-significant at the 95% CI) and $+0.0132 \cdot SAOD_{550}$ units per ONI unit ($R^2$ = 0.0566, non-significant at the 95% CI); conversely, decreasing trends are noticed for the other two factors, with $-0.0066 \cdot DAOD_{550}$ units per ONI unit ($R^2$ = 0.1859, significant at the 95% CI) and $-0.0007 \cdot AAOD_{550}$ units per ONI unit ($R^2$ = 0.1506, significant at the 95% CI). Nevertheless, these trends are considered quite low or even neutral, but they agree in the sign completely with the correlation coefficients between these factors and ONI as shown above (positive for $TAOD_{550}$ and $SAOD_{550}$, negative for $DAOD_{550}$ and $AAOD_{550}$). Therefore, the results show that the ENSO phenomenon is likely to have a greater impact on the dispersion of dust aerosols and the dominance of absorbing particles over the wider Mediterranean region than the scattering effect of these on solar radiation. This outcome is in agreement with a similar observation by Urdiales-Flores et al. [32], who did not associate the declining trend in TAOD550 over the region with a significant effect of ENSO. Ruckstuhl et al. [73] also showed that, apart from the period 1991–1994, coinciding with the effect from the Pinatubo volcano eruption, $TAOD_{500}$ shows a declining trend over Europe in the period 1981–2005.

Another quantity that represents the size of aerosols is the Ångström exponent ($AE_{470–870}$). Figure 6 displays a plot that is comparable to the one in Figure 5. The distribution of the data pairs ($AE_{470–870}$, ONI) is shown here. It is observed that, regardless of the ENSO phase, all cases show coarse-mode particles across the Mediterranean on a yearly basis. Fine-mode aerosols are linked to only two years, 1983 and 1992, related to volcanic eruptions. The Earth's atmosphere, including the Mediterranean, was inundated by fine-mode particles, which persisted in the atmosphere even a year after the massive volcanic eruptions of Mt. El Chichón in Mexico (28 March–4 April 1982) and Mt. Pinatubo in the Philippines (12–15 June 1991). Mt. El Chichón injected $7 \times 10^6$ tonnes of sulphur dioxide ($SO_2$) and $20 \times 10^6$ tonnes of particulate matter into the stratosphere [74]. The eruption occurred just as the 1982–1983 El Niño event was in its starting phase; because of this, some scientists have suggested that the El Chichón eruption triggered a positive El Niño phase [74]. Nevertheless, climate models and detailed studies of past volcano eruptions and El Niño events have not shown a connecting line between the two events, and therefore the timing must be just a coincidence [74]. On the other hand, the Pinatubo eruption released a huge amount ($17 \times 10^6$ tonnes) of $SO_2$ into the stratosphere, causing a global temperature decrease of 0.4 °C [75] and a reduction in solar light by 10% (http://www.cmdl.noaa.gov/albums/cmdl_overview/Slide18.sized.png (accessed on 15 January 2024)).

The average annual $AE_{470–870\ value}$ over the Mediterranean and over the period under investigation for the current work is 0.939, which is comparable to the values of 1.15–1.66 discovered for the eastern Mediterranean during the period 1999–2018 by Ozdemir et al. [69]. Sharafa et al. [76] found, from AERONET stations, average annual $AE_{470–870}$ values in the range of 0.555–1.722 in three sub-Saharan African countries in the period 2000–2015. As far as the correlation of $AE_{470–870}$ with ENSO in the present study is concerned, it was found that $r_{AE470–870,ONI}$ = +0.349 ($p$ = 0.022 < 0.050, significant at the 95% CI). Mallet et al. [72] found $AE_{440–870}$ to fluctuate between 0.92 and 1.57 over the Mediterranean region in the period 1996–2012 (mostly within 2003–2012); these values are consistent with those found in the present work (0.76–1.56).

### *3.2. ENSO and Cloud Properties*

Clouds play a significant role in (i) the Earth's energy balance by either reflecting solar energy back to space (cooling effect) or reflecting the infra-red (IR) energy emitted from the surface of the Earth back to the surface (warming effect); (ii) climate change due to the above cooling or warming effects; (iii) the planet's albedo, which is modified in cases of heavy, thin, or absence of cloudiness; (iv) global precipitation patterns; and (v) the formation/modification of clouds when aerosols like volcanic ash and air-pollution

particles act as cloud condensation nuclei. One of the measures for the activity of clouds is COD, which is a quantity interpreted as the attenuation that clouds exert on solar radiation. COD can range from almost 1 to 100 [77], depending on the texture, vertical development, and water content of the clouds. Figure 7 shows the variation of the cloud thickness over the Mediterranean as a function of ONI. It is evident that the COD values are not prioritised based on the ENSO phase (positive, neutral, or negative). The dispersion of the (COD, ONI) data pairs is rather uniform in the whole ONI range (−1.5, +1.5). This is to be expected, because Section 3.1 on aerosol-quantified attributes showed no discernible reliance on ONI; as previously stated, aerosols have the ability to modify clouds, implying that ENSO has a completely indirect effect on clouds, if any.

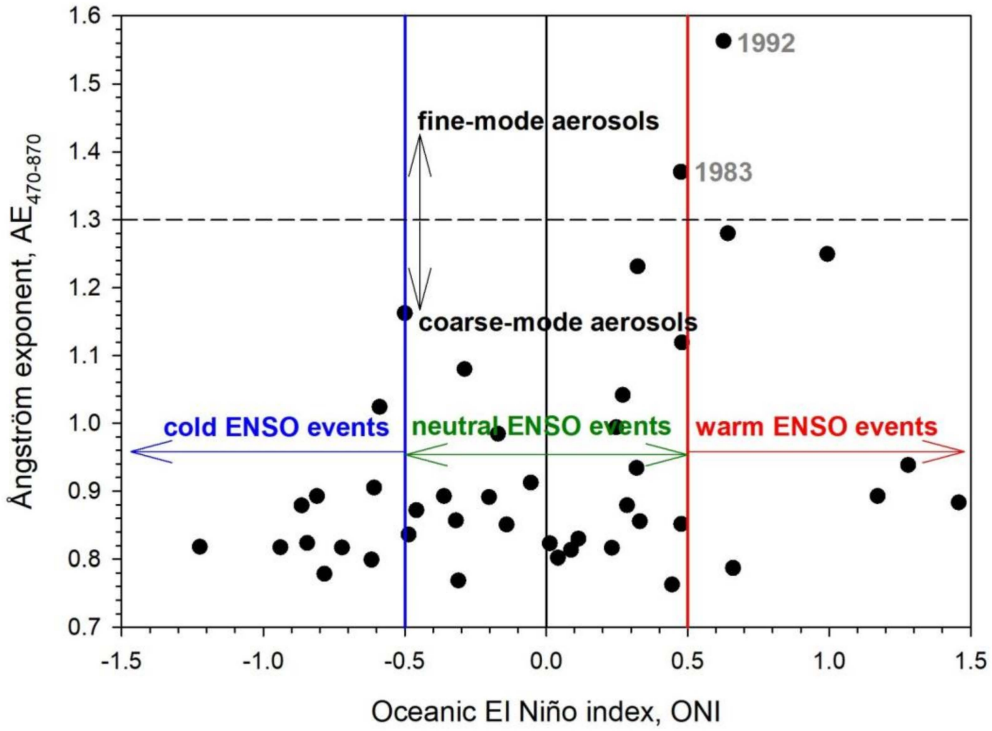



**Figure 6.** Annual mean values of $AE_{470–870}$ over the selected domain in the Mediterranean region versus ONI in the period 1980–2022. The zone constrained by the blue and red vertical lines includes neutral ENSO events only. ONI values equal to or greater than +0.5 denote (warm) El Niño cases and equal to or less than −0.5 (cold) La Niña events. The horizontal dashed line denotes the threshold of $AE_{470–870}$ = 1.3; aerosol particles with $AE_{470–870}$ > 1.3 are characterised as fine mode, and $AE_{470–870}$ < 1.3 as coarse mode. The data points denoted as 1983 and 1992 correspond to the El Chichón and Pinatubo eruptions, respectively.

The annual average value of COD in the present study is 17.87 for the whole Mediterranean. Luccini et al. [78] found COD values of ≈15 (at Arica) and ≈11 (at Poconchile) in the Atacama Desert in northern Chile. The COD values also reflect the frequency of cloudiness occurrence over an area (lower values over a desert, higher ones over the Mediterranean, including vegetated and water surfaces).

### *3.3. ENSO and Atmospheric Radiation*

The dependence of SSN, $netSW_{BOA}$, $netLW_{BOA}$, and DARF on ONI is covered in this section. The first parameter's correlation with the ENSO phenomenon is of general interest because it indicates whether there is an interdependence between the two parameters (see Figure 8a); the second parameter, the net solar radiation (incident—reflected) at BOA, is expected to be influenced by ENSO due to the atmospheric aerosols' attenuation of solar light, which showed a (loose) dependence on ENSO, particularly in cases of volcanic eruption (see Figure 8b); the third parameter is the net IR radiation (incident—reflected)

at BOA (see Figure 8c); the last parameter is the atmospheric aerosol forcing within the Mediterranean atmosphere (i.e., from TOA to BOA), and it is interesting to investigate whether there is a teleconnection with ENSO (see Figure 8d). Both netSW and netLW have been considered at BOA in clear-sky conditions and with aerosols in the atmosphere; clear skies were chosen so that any implication from clouds be avoided while examining the effect of ENSO on the aerosols' radiative forcing and, therefore, on the global warming phenomenon in the Mediterranean region.

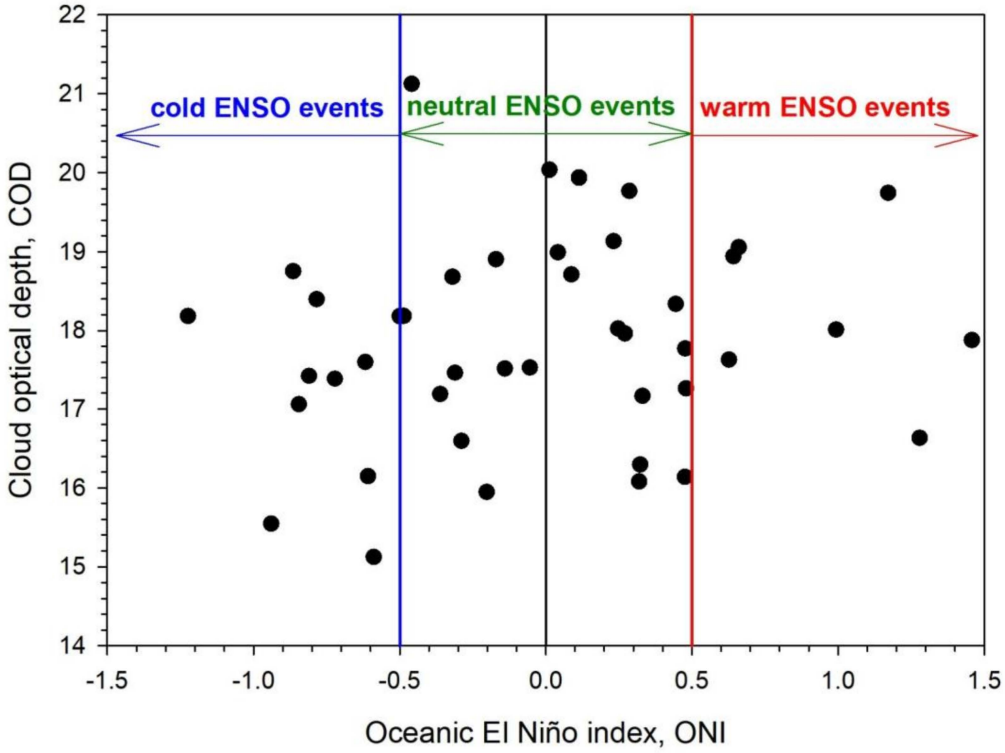
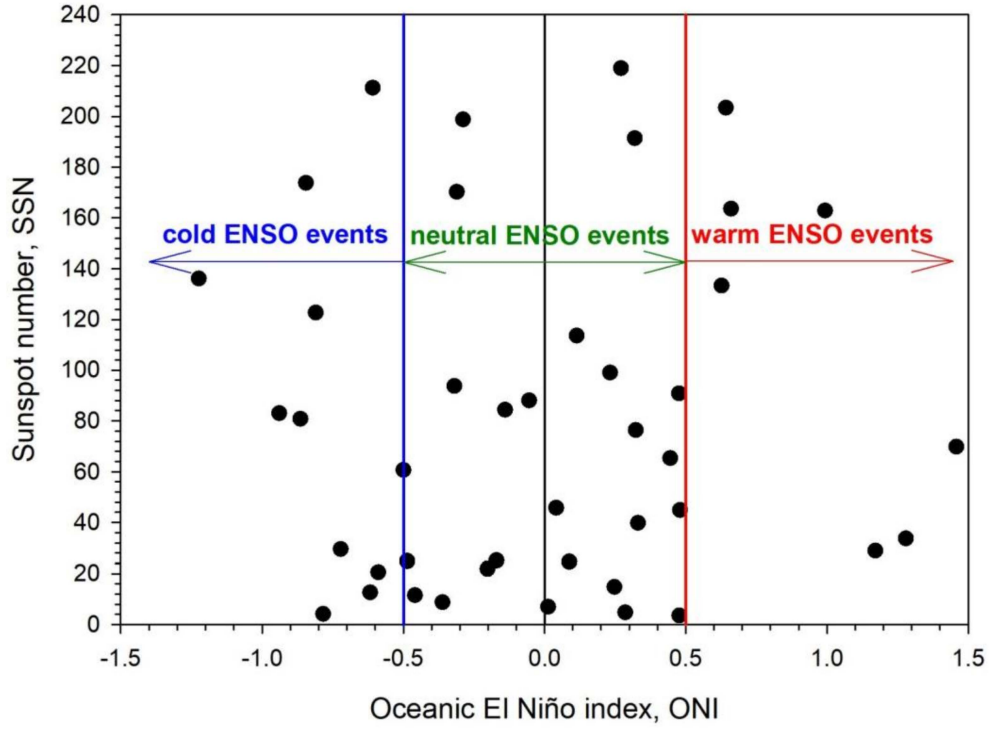



**Figure 7.** Average annual COD values over the selected domain in the Mediterranean region for various ENSO events in the period 1980–2022. The zone constrained by the blue and red vertical lines includes neutral ENSO events only. ONI values equal to or greater than +0.5 denote (warm) El Niño cases and equal to or less than −0.5 (cold) La Niña events.

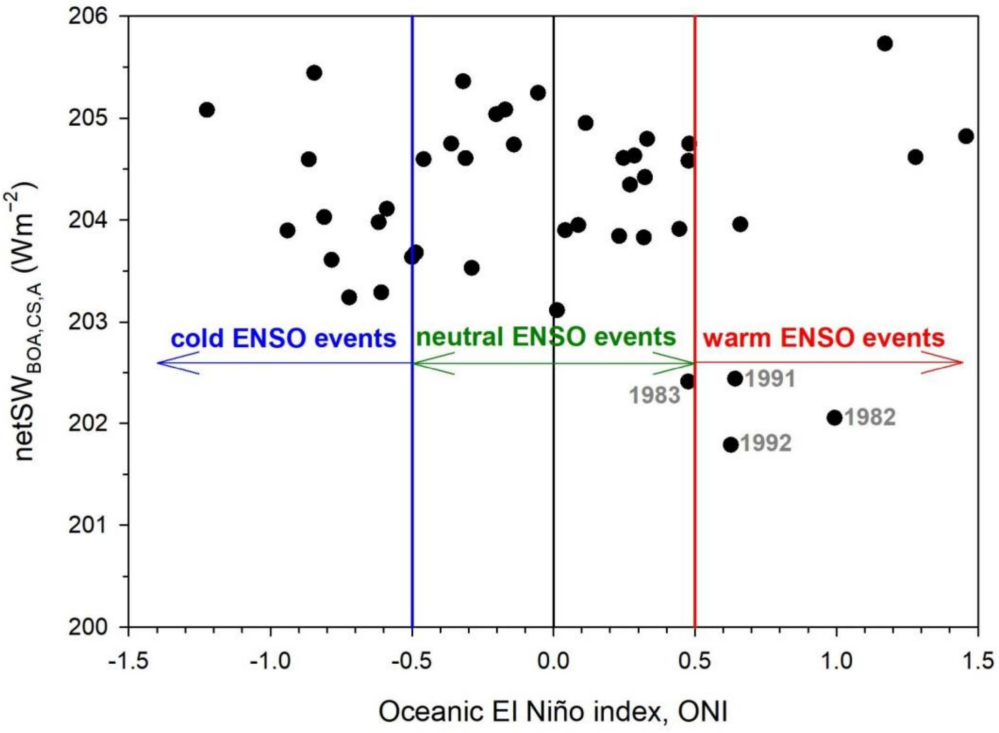
Over the selected domain of the Mediterranean and during the studied period, the average values of $netSW_{BOA,CS,A}$ and $netLW_{BOA,CS,A}$ are +204.16 $Wm^{-2}$ and −97.93 $Wm^{-2}$, respectively. The minus sign in the $netLW_{BOA,CS,A}$ indicates an upward orientation, thus implying that the Mediterranean region emits more upward IR radiation from the surface than is absorbed by the atmosphere. This finding may be related to the aerosol-induced global warming in the area; further analysis of this will be provided in the following section.

The sunspot number in Figure 8a shows a great dispersion with respect to the ENSO phases; therefore, no preference in the ENSO phase is shown for SSN $\leq$ 50 (low solar activity [79]), at least in the examined period of 1980–2022. However, the graph indicates a preference of ONI $\leq$ +0.5 for SSN < 120 sunspots. This outcome requires more research in order to determine whether these observations are random coincidences.

The net solar irradiance at the surface of the Earth under clear skies and in an aerosol-laden atmosphere in Figure 8b shows a rather compact dispersion around values lying between +202 $Wm^{-2}$ and +206 $Wm^{-2}$; the years with volcanic eruptions are clearly marked (1982–1983 for El Chichón, 1991–1992 for Pinatubo). Another interesting feature is the dispersion of the majority of the ($netSW_{BOA,CS,A}$, ONI) data pairs for ONI $\leq$ +0.5; such a conclusion was drawn for $AOD_{550}$, as shown in Figure 5, demonstrating the effect of the atmospheric aerosols on solar radiation.

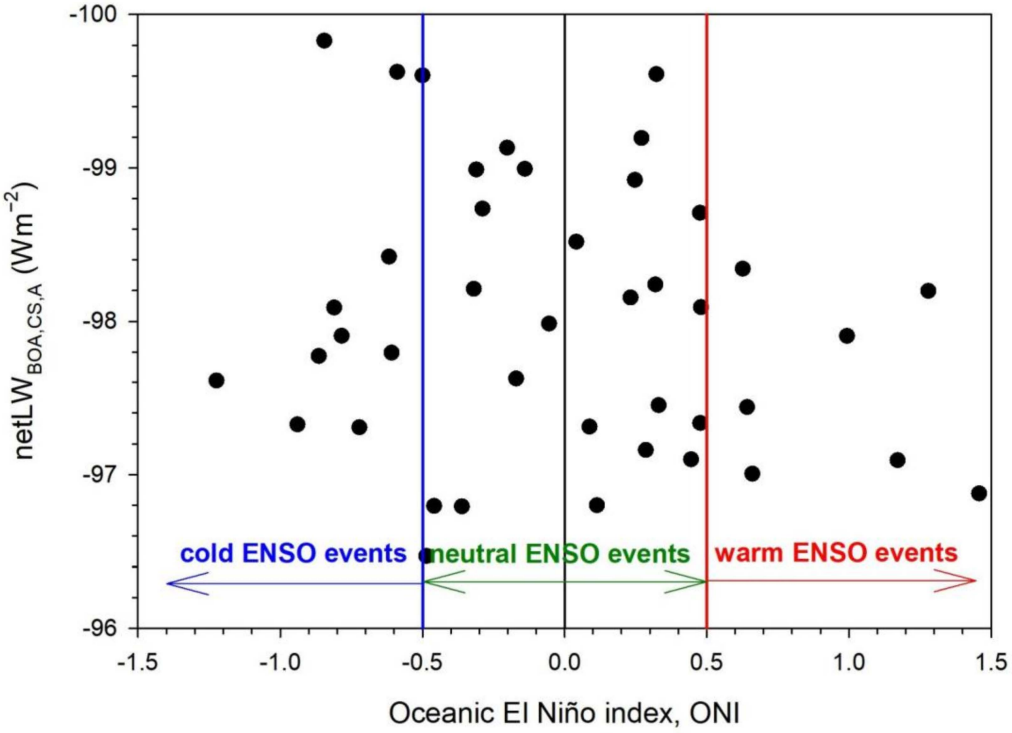



(**a**)

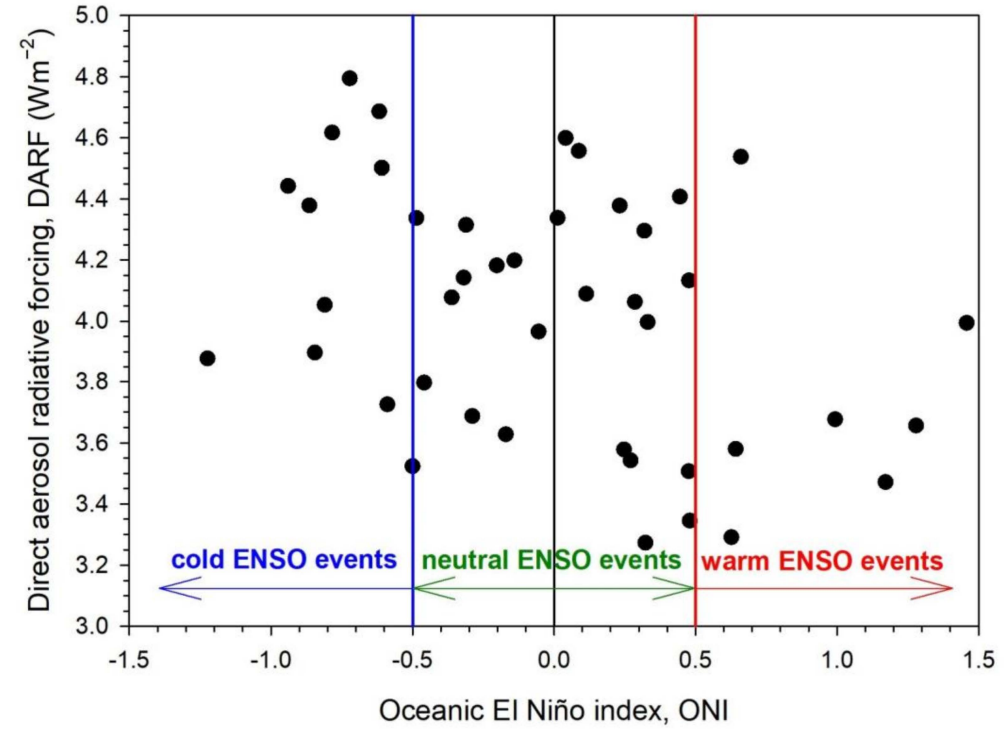



(**b**)

**Figure 8.** *Cont.*




(**c**)




(**d**)

**Figure 8.** Average annual values of (**a**) SSN, (**b**) netSW$_{BOA,CS,A}$ (in Wm$^{-2}$), (**c**) netLW$_{BOA,CS,A}$ (in Wm$^{-2}$), and (**d**) DARF (in Wm$^{-2}$) over the selected domain in the Mediterranean region for various ENSO events in the period 1980–2022. The zone constrained by the blue and red vertical lines includes neutral ENSO events only. ONI values equal to or greater than +0.5 denote (warm) El Niño cases and equal to or less than −0.5 (cold) La Niña events.

Similar to the net solar irradiance, the net IR radiation at the Mediterranean surface displays a dispersion between ≈−96.5 $Wm^{-2}$ and ≈−100.0 $Wm^{-2}$, with a bias for ONI ≤ +0.5 values (Figure 8c).

The range of DARF in Figure 8d is from ≈+3.2 $Wm^{-2}$ to ≈+ 4.8 $Wm^{-2}$; an existing, though hazy, declining trend in DARF from negative to positive ONI levels can be observed. This result may be linked to the behaviour of $netSW_{TOA,CS,A}$ and $netLW_{TOA,CS,A}$, which is similar to that of DARF in terms of dispersion and trend. This indicates that the Mediterranean region is subject to a (loose) influence of ENSO on atmospheric radiation throughout the entire depth of the atmosphere.

### *3.4. Additional Analysis*

This section contains information not belonging to the previous groups of results. It is intended to present the inter-annual variation of the examined parameters over the broader Mediterranean area in the period of the study.

Figure 9 shows the inter-annual variation of DARF over the selected domain of the Mediterranean in the studied period. An increasing trend is obvious. From the expression for the linear fit to the DARF values shown in the legend of Figure 9, one can easily compute $DARF_{2022}$ = +45.6271 $Wm^{-2}$, and $DARF_{1980}$ = +44.7535 $Wm^{-2}$; then, ($DARF_{2022}$−$DARF_{1980}$)/4.3 = +0.203 $Wm^{-2}$ per decade (43 years in 1980–2022 represent 4.3 decades); this finding indicates a slow warming effect in the last 4 decades, as the net radiation at TOA is greater than that at BOA (see Equation (1)), thus resulting in a positive signal. During the studied period, the average DARF value is +4.026 $Wm^{-2}$, which is relatively near to +4.503 $Wm^{-2}$ for the Mediterranean as found by Korras-Carraca et al. [80] in the period 1980–2019. Comparable findings have been obtained by Kambezidis and Kampezidou [81] and Kambezidis et al. [82] in two studies about the global dimming/brightening effect of aerosols over the Mediterranean Sea in the period 1979–2012. Papadimas et al. [83], on the other hand, obtained an average DARF ($DRE_{atm}$ in their paper) of +14.3 $Wm^{-2}$ over the Mediterranean in the period 2000–2007, a value much higher than the one found in the present study (cf. +4.026 $Wm^{-2}$). The positive sign in the overall DARF means that the net radiation at TOA surpasses that at BOA (mathematical interpretation by Equation (1)). This can be explained by minimising the difference $(Q_A - Q_{NA})_{BOA}$ in Equation (1), a fact that implies that the net radiation with the presence of aerosols is comparable to that without aerosols at the bottom of the atmosphere over the Mediterranean. This outcome can be attributed to lower air-pollution levels achieved by adopted abatement policies within most of the European Union's member countries, with a cleansing effect on the atmosphere above the Mediterranean region. It is interesting to observe that the correlation $r_{DARF\text{-}SSN}$ in the whole period of the study is −0.138 ($p$ = 0.379 > 0.050, non-significant at the 95% CI), while in the sub-periods 1980–2000 and 2001–2022, it is +0.401 ($p$ = 0.401 > 0.050, non-significant at the 95% CI) and −0.034 ($p$ = 0.880 > 0.050, non-significant at the 95% CI), respectively. Also, the correlation $r_{DARF\text{-}ONI}$ in the whole period of the study is −0.391 ($p$ = 0.010 < 0.050, significant at the 95% CI), while in the sub-periods 1980–2000 and 2001–2022, it is −0.486 ($p$ < 0.010, significant at the 99% CI) and −0.466 ($p$ = 0.029 < 0.050, significant at the 95% CI), respectively. On the other hand, SSN shows a declining trend within the studied period, with a rate of −2.45 sunspots per year or −24.5 sunspots per decade. This decreasing trend in the solar activity has been noticed by various astrophysicists, e.g., [82,84,85]. The above results lead to the following conclusions.

1. There is a medium negative correlation (anti-correlation) for the DARF-ONI time series in the sub-periods 1980–2022, and 2001–2022, while there exists a medium positive and a low negative correlation in the (DARF, SSN) pair in the mentioned sub-periods, respectively.
2. During the 1980–2000 sub-period, there is a high positive and a negative correlation for the DARF-SSN and DARD-ONI time series, respectively.

3. The first sub-period includes both volcanic eruptions mentioned above, which sent vast amounts of ash and gases into the atmosphere and affected the atmospheric radiation budget over the Mediterranean.
4. From 2000 onward, the 11-year solar activity has been progressively decreasing, with a solar minimum predicted for roughly 2040–2050 [79] (current solar cycle 25), which is anticipated to have a further impact on the atmospheric radiation and aerosol properties over the Mediterranean region.
5. There is a solar brightening signal over the Mediterranean after the 1990s [82,86–89]. It is obvious that reduced surface temperatures and decreased water evaporation may follow lower solar radiation levels; these factors may have led to decreased cloud cover and precipitation [82,90]. Moreover, reduced precipitation indicates less frequent aerosol washout, which increases the number of suspended particles in the atmosphere. These particles may increase solar light absorption, which can, in turn, slow the warming effect over the Mediterranean (see the slight increasing trend of $AAOD_{550}$ in Figure 12).

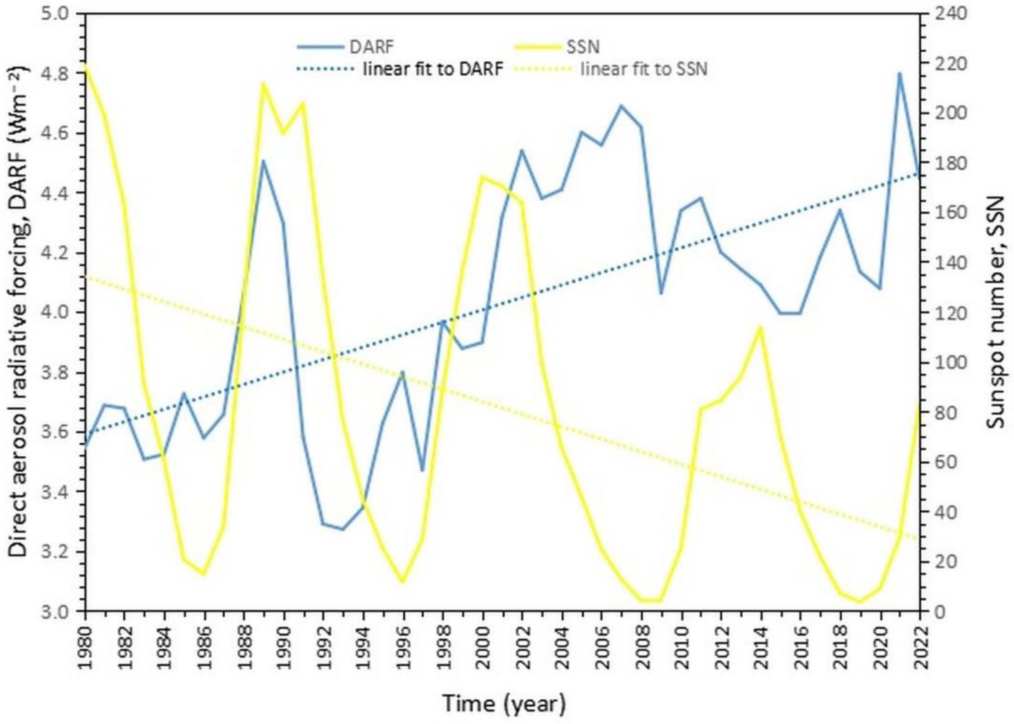



**Figure 9.** Variation in the annual mean values of DARF (blue solid curve) over the selected domain in the Mediterranean region and of SSN (yellow solid curve) in the period 1980–2022. The linear fit to the DARF values (dotted blue line) is expressed by the equation DARF = 0.0208·t + 3.5695 with $R^2$ = 0.3945, significant at the 99.9% CI, and to the SSN values (dotted yellow line) by the expression SSN = −2.5084·t + 136.5500 with $R^2$ = 0.2217, significant at the 95% CI; t is any year within the examined period.

Figure 10 shows the inter-annual variation of $netSW_{BOA,CS,A}$ and $netLW_{BOA,CS,A}$. Since both of these parameters have a substantial impact on the solar radiation climate (and hence the energy budget) of the Mediterranean, the graph shows how these parameters have been changing over time. There has been an upward tendency in both radiation fluxes over time. After doing the same basic calculations as for the DARF instance above, it is possible to determine from the linear regression equations provided in the legend of Figure 10 that netSW and netLW have increasing trends of +0.207 $Wm^{-2}$ and +0.621 $Wm^{-2}$ per decade, respectively. From these results, we can draw the following conclusions according to the definition of the net flux given in Equation (4).

1. A slight increase in netSW = SW↓ − SW↑ means that the difference between the two SW fluxes increases with time, but the reflected SW radiation (SW↑) increases at a slower pace than its downward counterpart (SW↓). This could be the result of a change (decrease) in the overall surface albedo ($\rho_g$, land and sea) over the selected Mediterranean area in the period 1980–2022, reflecting less and less SW over time; however, this is not the case, as shown by the red solid line in Figure 2, which shows a rather steady state for $\rho_g$ over time. Therefore, the cause must be sought in the increase in SW↓ (not shown here, but mentioned in various studies, e.g., [91]).
2. The netLW flux shows the same trend as the netSW; an increase in netLW over time may be linked to a decreasing LW↑, which may be explained by a decrease in the surface's emissivity in the Mediterranean region, or a decrease in $\rho_g$, which is not the case in this instance (see Figure 2; also explained in item 1 above). Therefore, the explanation is an increased rate in the downward IR flux, which suggests a warming signal over the Mediterranean, in accordance with the conclusion at the beginning of this section.
3. The energy budget (netSW + netLW) at the surface of the Mediterranean (land and sea) seems to change over time, being more and more in the IR band; indeed, from the regression expressions for netSW and netLW in the legend of Figure 10, it is estimated that $netSW_{2022} - netSW_{1980} = +0.890\ Wm^{-2}$, and $netLW_{2022} - netLW_{1980} = +2.672\ Wm^{-2}$. This leads to an increase of $netSW_{1980–2022} + netLW_{1980–2022} = +3.562\ Wm^{-2}$ or $+0.828\ Wm^{-2}$ per decade. The increase in the netLW flux over the whole Mediterranean region is a sign of regional warming in the presence of atmospheric aerosols and clear skies. A study by Kambezidis et al. [82] for the Mediterranean area in the period 1979–2012 showed a slight decreasing trend in $netSW_{BOA,CS,A}$ of $-0.17\ Wm^{-2}$ per decade, which does not agree with the slight increase of $+0.621\ Wm^{-2}$ per decade in the present work; the disagreement may be attributed to the further recovery of the solar radiation levels (brightening effect) in the decade 2013–2022.

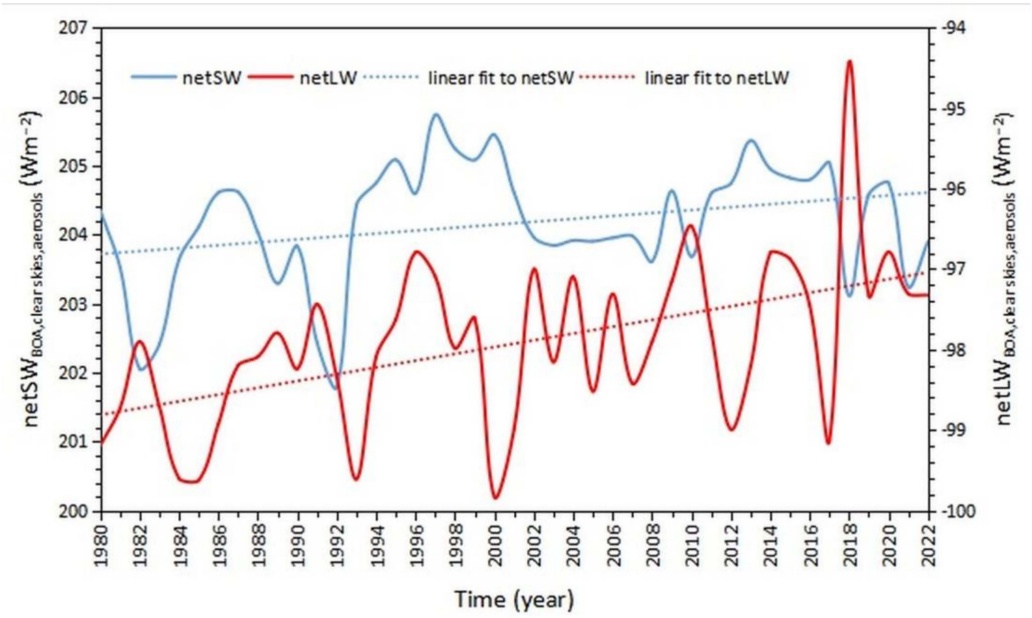



**Figure 10.** Variation in the annual mean values of netSW (blue solid curve) and netLW (red solid curve) over the selected domain in the Mediterranean region in the period 1980–2022. Both fluxes are considered at BOA with the presence of atmospheric aerosols in the atmosphere. The linear-fit expressions are netSW = 0.0212·t + 161.6549 with $R^2 = 0.089$, and netLW = 0.0422·t – 182.3030 with $R^2 = 0.261$, with both expressions being non-significant at the 95% CI; t is any year within the examined period.

The above conclusions can be related to the time evolution of the COD time series over the selected Mediterranean area in the examined period of the study; this evolution is shown in Figure 11. The correlation coefficients among the annual mean values of the parameter pairs examined so far are $r_{DARF\text{-}COD} = +0.095$ ($p = 0.544 > 0.050$, non-significant at the 95% CI), $r_{netSW\text{-}COD} = +0.226$ ($p = 0.145 > 0.050$, non-significant at the 95% CI), and $r_{netLW\text{-}COD} = +0.545$ ($p < 0.001$, significant at the 99.9% CI). The higher value of $r_{netLW\text{-}COD}$ suggests a greater dependence of the IR radiation on cloudiness than the SW one. Moreover, the small correlation coefficient between DARF and COD indicates an insignificant dependence of the direct aerosol radiative forcing on cloudiness. The latter is explained by the fact that clouds are formed up to 15 km above the Earth's surface, whereas DARF refers to the entire depth of the atmosphere, which is typically 100 km. As a result, there is a loose affinity between the two factors.

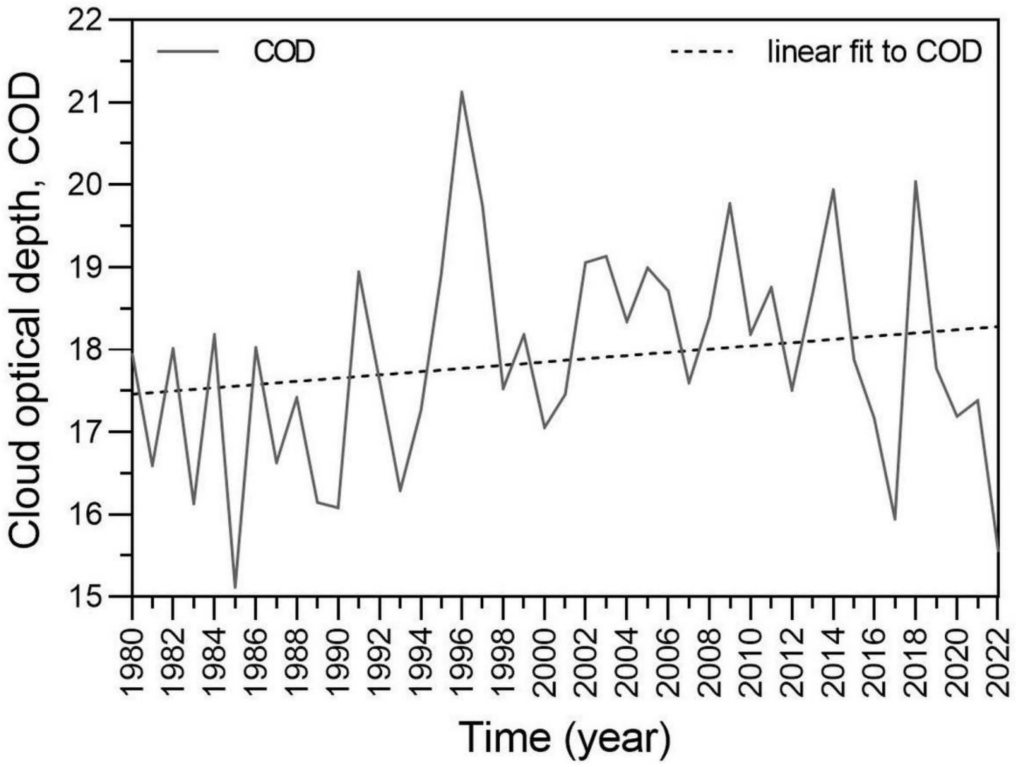



**Figure 11.** Variation in the annual mean COD values across the selected domain in the Mediterranean region in the period 1980–2022. The linear-fit expression is $COD = 0.0195 \cdot t + 17.4410$ with $R^2 = 0.0360$, non-significant at the 95% CI; t is any year within the examined period.

The increasing trend in COD as shown in Figure 11 indicates a progressive increase in cloudiness (both in clouds height and texture, i.e., water content) over time in the selected Mediterranean region. Indeed, Katsoulis and Kambezidis [92] found a 2.8% increase in cloudiness and a 2% decrease in sunshine duration over Greece in the period 1950–1984. Founda et al. [93] also revealed an increase in the frequency of the cloud-cover occurrence of 0.124% per year over Athens in the period 1882–2012 during a typical day of the year (see their Table 1 and Figure 1e); however, they found a significant increase for low clouds, especially after the mid-1980s, a prominent decrease in middle clouds, and a smoother increase in high clouds from 1882 until the late 1980s. On the other hand, Ioannidis et al. [90] found a decrease in the total cloud cover over the Mediterranean–Black Sea region in the period 1970–2014 and attributed it to the strong cloud-cover decrease from late autumn to early spring in next year. This observation is in line with the decrease in COD (all cloud types included) over the Mediterranean found by Kambezidis et al. [82]. Nevertheless, the latter researchers stated that the trend in COD is not uniform throughout the Mediterranean nor within the year (see their Figures 10 and 11) and attributed these alterations

to the variability in the atmospheric aerosol loading over the various locations in the area. The overall increase in COD computed from the linear-fit expression in the legend of Figure 11 is +0.19 per decade in the period 1980–2022 (or +0.34% per decade), a small increase, almost negligible if compared to the great annual COD values (about 17). This means that it is not certain that the overall cloudiness (all types of clouds) demonstrates an apparent decrease or increase. With respect to this, Norris and Wild [94] computed the COD trend over Europe from 1971 to 2002 using the GEBA network. They discovered that it was +0.9% per decade (1987–2002), which is significantly higher than the +0.34% per decade obtained in the current study. What is apparent is that, regardless of the kind or degree of cloudiness, COD seems to be trending as somewhat increasing. COD plays a significant role in the attenuation (scattering or absorption) of solar radiation and consequently results in a cooling or warming impact on the Mediterranean. Furthermore, significant year-to-year variations in COD are seen in Figure 11 for the period 1980–2022, with a declining tendency after 2018. This negative tendency does not appear to have had a significant impact due to the short duration of the COD trend computation relative to the entire study period, when contrasted with the increases by the cited studies computed over shorter time intervals than the one in the current work. The information above leads one to the conclusion that there is no guarantee that the total amount of cloudiness, including all kinds of clouds, has decreased or increased.

The next item to be looked into is the time evolution of all kinds of $AOD_{550}$ ($TAOD_{550}$, $SAOD_{550}$, $AAOD_{550}$, $DAOD_{550}$) over the selected Mediterranean region. Averaged spatial values are displayed in Figure 12. $TAOD_{550}$ and $SAOD_{550}$ exhibit a strong downward trend, $DAOD_{550}$ shows a moderate upward trend, and $AAOD_{550}$ shows little change. From the regression equations in the legend of Figure 12, it is found that the change in $TADO_{550}$ is $-0.0182$ per decade; in $SAOD_{550}$, $-0.0187$ per decade; in $DAOD_{550}$, $+5.5814 \times 10^{-4}$ per decade; and in $AAOD_{550}$, $+7.6744 \times 10^{-4}$ per decade. These values correspond to changes of $-7.21\%$ per decade, $-7.73\%$ per decade, +5.53% per decade, and +0.88% per decade, respectively. For both TAOD and SAOD, Figure 12 depicts a rapid falling tendency; this is misleading, since the decadal changes are orders of magnitude smaller than the actual values. The growing inclinations of DAOD and AAOD are comparable and more grounded in reality. Nevertheless, compared to the downward trend in scatterers (SAOD) in the atmosphere, the upward trends in DAOD and AAOD suggest an increasingly larger rise in dust and absorbing particles. A recent study also noted the declining trend in TAOD over the Mediterranean [32]. Raptis et al. [95] found a $-1.7\%$ trend per year for $TAOD_{440}$ over Athens, Greece, in the period 2008–2018; this value is $-0.72\%$ per year in our case. Nabat et al. [96] mentioned an AOD trend of $-0.07$ per decade for central Europe in the period 1980–2009, a value almost seven times higher than the one computed in the present study ($-0.0182$ per decade). Chiapello et al. [70] found a $TAOD_{550}$ trend of $-0.06$ per decade for the western Mediterranean in the period 2005–2013, which is almost six times higher than the value in the present work. Mallet et al. [72] found $AAOD_{440}$ values over the Mediterranean in the period 2000–2009 of $\approx$0.05 under the influence of dust aerosols. $AOD_{440}$ values for the same area under the auspices of various experimental campaigns show mean values ranging between 0.15 and 0.32, depending upon the region of the Mediterranean (see Table 1 in [72]). These values are fairly similar to the annual mean $TAOD_{550}$ of 0.213 in the present study. A recent study on the atmospheric aerosols over a wide area that included northern Africa, the Middle East, and Asia [97] used data from AERONET stations; especially for northern Africa, which constitutes part of the domain examined in the present study, three sites (Tamanrasset in Algeria, Medenine in Tunisia, and Cairo in Egypt) showed average $AOD_{500}$ values of 0.29, 0.30, and 0.50, respectively. These values were linked to frequent dust events over these places, as they are higher than the value of 0.213 observed here for the Mediterranean. Conversely, Pace et al. [98] discovered an average value of 0.24 for $TAOD_{495.7}$ from their own radiometer measurements made during the period of July 2001 to September 2003 on the Italian island of Lampedusa; this result is very close to our average of 0.213. Urdiales-Flores et al. [32]

investigated the drivers that are causing a warming acceleration over the Mediterranean in the last 120 years and found a combined effect of declining AOD and decreasing soil moisture. Their conclusion is in accordance with the declining trend in $TAOD_{550}$ shown in Figure 12 of the present study.

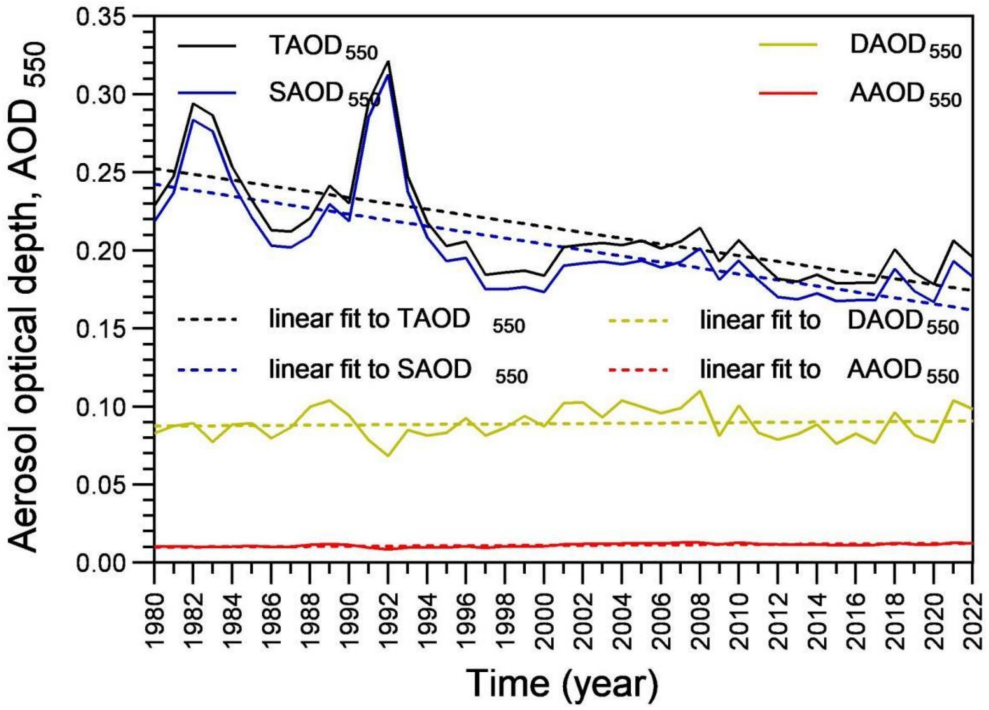



**Figure 12.** Variation in the annual mean $AOD_{550}$ values across the selected domain in the Mediterranean region in the period 1980–2022. The linear-fit expressions are $TAOD_{550} = -1.8610 \times 10^{-3} \cdot t + 3.9370$ with $R^2 = 0.461$; $SAOD_{550} = -1.9190 \times 10^{-3} \cdot t + 4.0420$ with $R^2 = 0.475$; $DAOD_{550} = 7.6620 \times 10^{-5} \cdot t - 0.0642$ with $R^2 = 0.416$; and $AAOD_{550} = 5.7770 \times 10^{-5} \cdot t - 0.1043$ with $R^2 = 0.010$; t is any year within the examined period. All linear regression equations are significant at the 99.9% CI except for $AAOD_{550}$, which is not significant at the 95% CI.

A measure of the size of aerosols in the atmosphere is given by the Ångström exponent (see Equation (9)). In the VIS spectrum, this parameter is investigated between 470 and 870 nm ($AE_{470–870}$). Values greater than 1.3 characterise fine-mode aerosols; below this threshold, they are associated with coarse-mode particles. Figure 13 shows the time evolution of this parameter over the selected Mediterranean area in the period of the study. Though the AE has a negative trend, two peaks in 1983 and 1992 are related to the volcanic eruptions of El Chichón and Pinatubo, respectively, mentioned in Sections 3.1 and 3.3 Indeed, sulphate fine-mode particles overwhelmed the Earth's atmosphere for one full year after the eruptions (March 1982 for El Chichón and June 1991 for Pinatubo). Apart from these two distinct events, the annual values of AE vary at low levels. Even so, after 2010 there were occasional spikes in finer-mode aerosols in the Mediterranean atmosphere; these can be linked to eruptions of active European volcanoes (Eyjafjallajökull in 2010, Grímsvötn in 2011, Bárðarbunga in 2014–2015, and Fagradalsfjall in 2022, all four in Iceland; Cumbre Vieja, Canary Islands, Spain, in 2021 [44]), but not with the massive material outflow that came from the El Chichón and Pinatubo volcanoes. From the linear regression equation in Figure 13, it is found that the trend of $AE_{470–870}$ over time in the Mediterranean region is −0.0843 per decade (−0.0084 per year) or ≈−7.5% per decade (≈−0.75% per year). To have a measure for comparison, it should be noted here that typical values of $AE_{470–870}$ range from two or greater for fresh smoke particles [99] to nearly zero for desert-dust aerosols [100]. From AERONET and MODIS data, Filonchyk et al. [101]

found an overall decrease in $AE_{470–660}$ of −0.017 per year over eastern Europe (Belarus, Bulgaria, Czech Republic, Hungary, Moldova, Poland, Russia, Slovakia, and Ukraine); this steep decline in AE in eastern Europe was attributed to the various environmental measures taken in the region. Various experimental campaigns at different Mediterranean sites and in different periods have found annual mean $AE_{470–870}$ values in the range of 0.92–1.57 (see Table 1 in [72]); the annual mean value in the present study is 0.94, well within the above range. The W-ICARB campaign [102] observed that a combination of different characteristics (sea and land, meteorology, air pollution, aerosol-mixing processes, e.g., coagulation, humidification) led to mean $TAOD_{500}$ and $AE_{470–870}$ values as high as 0.39 and 1.27, respectively. In the Naples area, Italy, Damiano et al. [103] found average $TAOD_{440}$ and $AE_{440–870}$ values of 0.16 and 1.26 (compared with the values of 0.213 and 0.94 in the present study). In Lampedusa, Italy, Pace et al. [98] discovered an average $AE_{440–870}$ value of 0.86 between 2001 and 2003, which is fairly close to our 0.94. In the domain studied in the present study, northern Africa was one of the wide geographic areas covered by a recent study by Samman and Butt [97] on atmospheric aerosols. Three sites (Tamanrasset in Algeria, Medenine in Tunisia, and Cairo in Egypt) presented average $AE_{470–870}$ values of 0.28, 0.45, and 0.49, respectively. Due to the frequent dust outbreaks over these sites, the estimated values are less than the one obtained for the selected Mediterranean region (0.94) in the present study and were attributed to coarse-mode dust particles. On the other hand, because of the impact of air-pollution particles in large urban agglomerations along the Mediterranean belt, the air throughout the region is characterised by finer-mode aerosols.

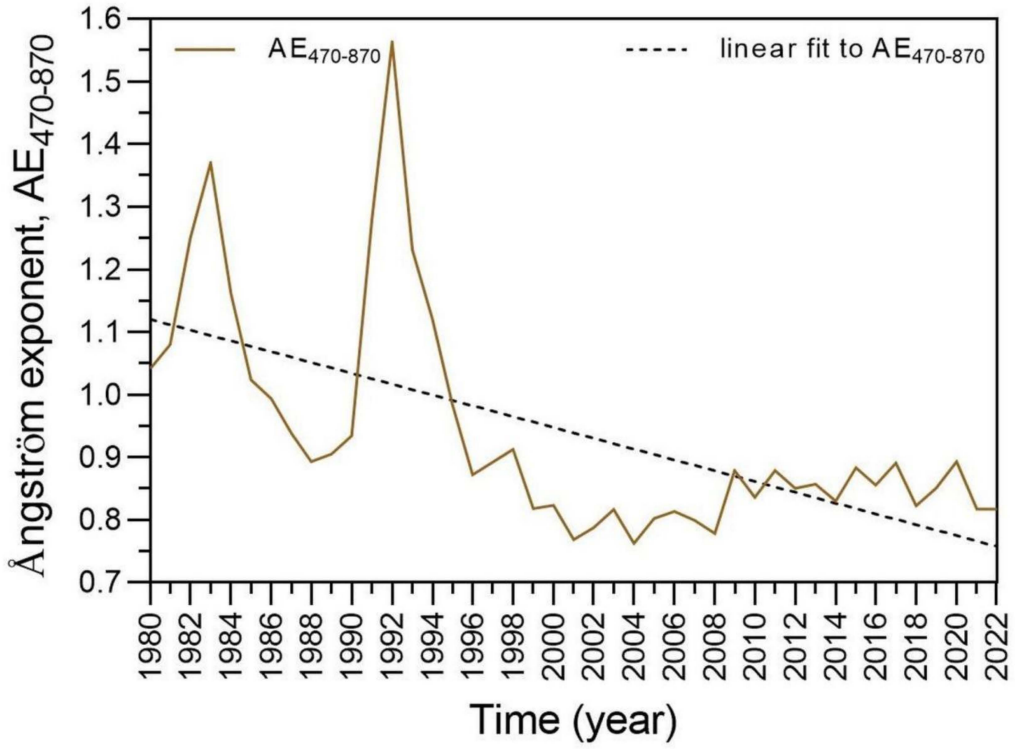



**Figure 13.** Variation in the annual mean $AE_{470–870}$ values across the selected domain in the Mediterranean region in the period 1980–2022. The linear-fit expression is $AE_{470–870} = -0.008634 \cdot t + 18.220000$ with $R^2 = 0.372$; t is any year within the examined period. The linear regression equation is significant at the 99.9% CI.

A last investigation concerns the type of aerosols present in the atmosphere of the Mediterranean in the period of the study. To categorise aerosols into groups, several researchers have developed varying ranges for the $TAOD_{550}$ and $AE_{470–870}$ values, e.g., [97,104–110]. The current investigation has adapted the aerosol-type discrimination criteria from [104]. These are (i) clean-maritime aerosols (CMAs) for $TAOD_{550} < 0.15$ and $AE_{470–870} < 1.30$; (ii)

urban/industrial/biomass-burning aerosols (UBAs) for $TAOD_{550} > 0.20$ and $AE_{470–870} > 1.00$; (iii) coarse-mode, including desert-dust aerosols (CDAs) for $TAOD_{550} > 0.25$ and $AE_{470–870} < 0.70$; and (iv) mixed-type aerosols (MTAs) elsewhere. The different colouration of the data points in Figure 14 indicates the various types of aerosols present over the selected Mediterranean region on a monthly basis between 1980 and 2022. Most of them fall into the MTA and UBA categories. The CMA is due to the large amount of water in the Mediterranean, whereas the UBA aerosols are related to air pollution over the large urban agglomerations along the Mediterranean Sea coast and sporadic summertime wildfires. On the other hand, the scatter plot shows only 18 months that are of the CDA type. The fact that these CDA months are exclusively springtime (April, May, and sometimes March or June, not explicitly shown here) is very interesting. This finding suggests that the aerosols in question are related to suspended dust aerosols from the Sahara; in relation to this kind of aerosol, similar conclusions were drawn by Kaskaoutis et al. [110] for Solar Village in Saudi Arabia and Kalapureddy et al. [104] for the Arabian Sea. The majority of the data points in Figure 14 represent the MTA type.

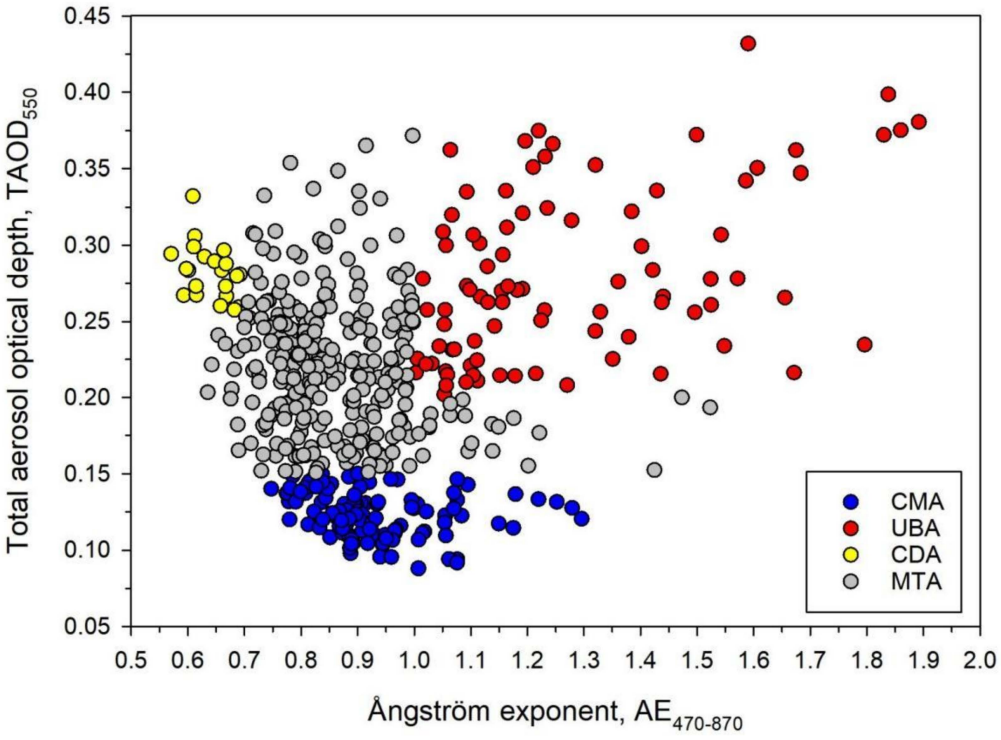



**Figure 14.** Scatter plot of the monthly mean ($TAOD_{550}$, $AE_{470–870}$) data pairs over the selected domain in the Mediterranean region in the period 1980–2022. The various types of aerosols are indicated by blue (clean-maritime aerosols, CMAs), red (urban/biomass-burning aerosols, UBAs), yellow (coarse-mode, including desert-dust aerosols, CDAs), and dark grey (mixed-type aerosols, MTAs).

### *3.5. Statistics*

This section contains the most important statistical results found in the previous sections. Table 2 refers to the correlation coefficients/coefficients of determination and the averages of the various parameters considered in this study. Table 3 displays the trends per decade for most of the parameters.

**Table 2. a.** Pearson's correlation coefficient (r) and coefficient of determination ($R^2$) between the time series of the parameters over the selected domain in the Mediterranean area in the period 1980–2022. The second parameter in each pair denotes the independent variable in the linear regression analysis. The asterisks beside the r or $R^2$ values denote significance at the 95% (*), 99% (**), or 99.9% (***) CI. **b.** Annual averages of the parameters over the selected domain in the Mediterranean area in the period 1980–2022. The averages are denoted by a bar over the parameter and refer to the whole period of the study and the selected Mediterranean area.

| **a. Parameter** | **r** | **$R^2$** |
|---|---|---|
| NAOI-ONI | +0.134 | 0.018 |
| NAOI-SSN | +0.211 | 0.045 |
| ONI-SSN | +0.021 | 0.000 |
| $TAOD_{550}$-ONI | +0.229 | 0.052 |
| $TAOD_{550}$-NAOI | +0.257 | 0.066 |
| $AE_{470–870}$-ONI | +0.349 * | 0.122 * |
| $AE_{470–870}$-NAOI | +0.289 | 0.084 |
| DARF-ONI | −0.391 ** | 0.153 ** |
| DARF-NAOI | −0.171 | 0.029 |
| netSW-ONI | −0.244 | 0.059 |
| netSW-NAOI | −0.241 | 0.058 |
| netLW-ONI | +0.144 | 0.021 |
| netLW-NAOI | +0.105 | 0.011 |
| COD-ONI | +0.143 | 0.020 |
| COD-NAOI | −0.093 | 0.009 |
| DARF-COD | +0.095 | 0.009 |
| netSW-COD | +0.226 | 0.051 |
| netLW-COD | +0.545 *** | 0.298 *** |
| **b. Parameter** | **Value** | |
| $\overline{NAOI}$ | +0.070 | |
| $\overline{ONI}$ | −0.008 | |
| $\overline{SSN}$ | +81.369 sunspots | |
| $\overline{TAOD_{550}}$ | +0.213 | |
| $\overline{AE_{470-870}}$ | +0.939 | |
| $\overline{DARF}$ | +4.026 $Wm^{-2}$ | |
| $\overline{COD}$ | +17.870 | |
| $\overline{netSW_{BOA,CS,A}}$ | +274.338 $Wm^{-2}$ | |
| $\overline{netLW_{BOA,CS,A}}$ | −97.928 $Wm^{-2}$ | |

**Table 3.** Trend per decade of the parameters used in this work. The trend refers to the whole period of the study and the selected domain in the Mediterranean area.

| **Parameter** | **Trend (Value per Decade)** |
|---|---|
| DARF | +0.203 |
| $netSW_{BOA,CS,A}$ | +0.207 $Wm^{-2}$ |
| $netLW_{BOA,CS,A}$ | +0.621 $Wm^{-2}$ |
| COD | −0.190 |
| $TAOD_{550}$ | −0.018 |
| $SAOD_{550}$ | −0.019 |
| $DAOD_{550}$ | $+5.281 \times 10^{-4}$ |
| $AAOD_{550}$ | $+7.674 \times 10^{-4}$ |
| $AE_{470–870}$ | −0.084 |

## 4. Discussion

The current study centred on the hypothesis of the extent to which the El Niño–Southern Oscillation influences various parameters of the atmospheric radiation over the wider Mediterranean region. The geographical coordinates of this area covered the latitudes 30° N–45° N and the longitudes 6° W–35° E. Almost all of Spain, the very south of France,

almost all of Italy, south Croatia, Bosnia-Herzegovina, Montenegro, Kosovo, northern Macedonia, three-quarters of Serbia, Greece, and Bulgaria, the very south of Romania, almost all parts of the Black Sea, a significant portion of Turkey, Cyprus, north-eastern Morocco, northern Algeria, Tunisia, the northern coasts of Libya, and Egypt, including the Sinai peninsula, and a significant portion of Israel were included in the selected area, which stretches from west to east and from north to south; of course, the selected domain included the entire Mediterranean Sea and the big islands of Corsica, Crete, Malta, Sardinia, and Sicily. All analyses treated this huge area as a single entity. This was done in an effort to address the question that was raised initially.

The findings of this work indicated that the ENSO phenomenon had a minimal impact on the optical characteristics of aerosols over the Mediterranean. A preference for greater TAOD and SAOD values under strong El Niño events is demonstrated in Figure 5; in contrast, dust (measured as DAOD) and absorbing (measured as AAOD) aerosols did not exhibit greater levels during all El Niño events. Additionally, under somewhat positive and significantly positive ONI values, a good mixing of aerosol sizes (in terms of AE) was seen (cf. Figure 6), whereas coarse-mode aerosols appeared to predominate under neutral and negative ONI values. The cloud optical depths showed a vague increasing trend from negative to positive El Niño events (cf. Figure 7). The direct aerosol radiative forcing showed a clear decrease from high (negative El Niño) to lower (positive El Niño) values (cf. Figure 8d); this outcome is the most important result of the study, as it shows that strong El Niño events provide a potential cooling over the Mediterranean region. This is demonstrated in Figure A1 of Appendix A. Regression expressions for the linear fits to the DARF and NAOI data points are also shown in the legend of the graph. These formulas show that there is a $-0.257$ Wm$^{-2}$ decrease in DARF for every ONI unit and an increase in NAOI of +0.082 units for every ONI unit. For these time series, their correlation coefficients are $r_{DARF\text{-}ONI} = -0.391$ and $r_{NAOI\text{-}ONI} = +0.134$. Accordingly, Figure A2 illustrates how $netSW_{BOA,CS,A}$ and $netLW_{BOA,CS,A}$ depend on ONI; the regression equations displayed in the legend of Figure A2 can be used to derive a trend of decreasing $netSW_{BOA,CS,A}$ of $-0.523$ Wm$^{-2}$ per ONI unit and increasing $netLW_{BOA,CS,A}$ of +0.235 Wm$^{-2}$ per ONI unit. These patterns demonstrate how ENSO occurrences indirectly affect the Mediterranean region's SW and LW radiation. For these time series, their correlation coefficients are $r_{netSWBOA\text{-}ONI} = -0.244$ and $r_{netLWBOA\text{-}ONI} = +0.144$.

From the analysis and the discussion, it appears that the initial hypothesis of a minor (indirect) ENSO influence on the atmospheric process (atmospheric radiation and aerosols) throughout the greater Mediterranean region is correct. Nevertheless, further research on this matter is required because more precise findings must be incorporated into general circulation models in anticipation of the upcoming publication of the IPCC report on the planet's changing climate. A future study might perform analyses on parts of the Mediterranean region in order to achieve better spatial resolution. Another idea might be to pursue analyses by considering negative, neutral, and positive El Niño events separately.

## 5. Conclusions

The primary goal of the study was to determine whether the ENSO large-scale event in the tropical Pacific has any potential influence, no matter how small, on some atmospheric radiation parameters over the Mediterranean region. The admission by many scholars, e.g., [110–113], that the Mediterranean is considered a hot spot on the Earth because of its location at the intersection of aerosol movements is what spurred this study. As a result, monthly mean data on solar activity (SSN), large-scale circulations (ENSO, NAO), aerosol properties ($AOD_{550}$, $AE_{470–870}$, COD), and surface albedo ($\rho_g$) over the chosen domain in the larger Mediterranean region were downloaded from various platforms between 1980 and 2022 (a period of 43 years). Additionally, the monthly mean DARF values were estimated from netSW and netLW values at both BOA and TOA. The following are, in brief, the primary conclusions drawn from this work.

1. As shown in Table 2a of Section 3.5, higher (positive) r values are shown between the optical aerosol properties ($TAOD_{550}$, $AE_{470–870}$) and either ONI or NAOI, and lower (negative) ones between the radiative parameters (DARF, $netSW_{BOA,CS,A}$) and either ONI or NAOI. Statistical significance was found between $netLW_{BOA,CS,A}$ and COD; this suggests that clouds play a significant role in preventing IR radiation from the ground (warming effect). Another interesting finding is the strong statistical significance of $AE_{470–870}$ or DARF with ONI, a fact that confirms the initial hypothesis of the influence of the ENSO phases on the size of the aerosol particles and their radiative effect over the Mediterranean region. Last, the very similar correlation coefficients of $TAOD_{550}$ and $netSW_{BOA,CS,A}$ with either NAO or ENSO give indirect evidence of the influence of ENSO on NAO and ultimately on the atmospheric radiation over the Mediterranean region.
2. As shown in Table 3 of Section 3.5, the highest positive trend is for the $netLW_{BOA}$ at the surface of the Mediterranean; this finding explains the positive trend of DARF (warming effect). Negative trends in the 43-year period of the study are shown by the COD, $TAOD_{550}$, $SAOD_{550}$, and $AE_{470–870}$ parameters; the trend of the latter parameter implies the predominance of coarser-mode particles in the atmosphere of the Mediterranean; these particles have a tendency to absorb solar radiation (positive trend of $AAOD_{550}$) rather than scatter it (negative trend of $SAOD_{550}$). This is so because the water droplets of clouds participate in and contribute to this mechanism (declining trend of COD). The trends in the studied parameters show how each parameter has evolved over the Mediterranean region in the period 1980–2022. Since the selected domain of the study is huge, the trends may be considered as being on a macro scale; nevertheless, they show a general trend (positive or negative) that agrees with that from other studies.
3. The majority of the atmospheric aerosols in the atmosphere of the selected Mediterranean region during the period of the study and on a monthly basis were found to be classified into the CMA and UBA categories; the first category is related to the vast water surface of the area, while the second is related to the air pollution in large cities and summertime wildfires.
4. There was a noticeable drop in the direct aerosol radiative forcing from cold to warm El Niño events (i.e., from negative to positive ONI values). This was shown by the significant negative correlation coefficient (−0.391) between DARF and ONI, which indicated that the progressive shift from cold to warm El Niño events is able to cause a cooling effect in the Mediterranean region, as expressed by DARF drifting to more negative values. This conclusion was confirmed by the significant positive correlation between $AE_{470–870}$ and ONI (+0.349); positive El Niño events tend to invoke fine-mode atmospheric aerosols over the Mediterranean, which are associated with a cooling effect. Furthermore, the El Niño phase has been shown to correlate positively with the North-Atlantic Oscillation (+0.134); it is, therefore, probable that the cooling effect is produced as a result of the ENSO–NAO teleconnection.
5. Though DARF's trend in relation to ONI is negative (see Figure A1), its trend with respect to time (years) is positive (see Figure 9). This outcome, strange at first glance, is quite explainable. The upward trend of DARF indicates that the atmosphere over the broader Mediterranean region gradually became warmer from 1980 to 2022. Nevertheless, on occasion, when the ENSO phase turns from positive to negative (from El Niño to La Niña) during one or two consecutive years, DARF shows lower values. The latter is shown in Figure A3.

**Funding:** This research received no external funding.

**Institutional Review Board Statement:** Not applicable.

**Informed Consent Statement:** Not applicable.

**Data Availability Statement:** Monthly data for netSW, netLW, AOD550, $AE_{470–870}$, and COD were downloaded from the Giovanni platform free of charge (access at https://giovanni.gsfc.nasa.gov/giovanni in the period 8–25 October 2023). Monthly data for NOAI and ONI were downloaded from the NOAA website free of charge (access at https://www.cpc.ncep.noaa.gov/products/precip/CWlink/pna/norm.nao.monthly.b5001.current.ascii.table for NOAI and https://origin.cpc.ncep.noaa.gov/products/analysis_monitoring/ensostuff/ONI_v5.php for ONI, in the period 8–25 October 2023). Monthly data for SSN were retrieved from the Royal Observatory of Belgium (ROB) free of charge (access at https://www.sidc.be/SILSO/datafiles on 18 October 2023).

**Acknowledgments:** The author is grateful to the personnel of GSFC/NASA, NPC/NCEP/NOAA, and ROB for preparing the databases used.

**Conflicts of Interest:** The author declares no conflicts of interest.

## Appendix A

This section provides additional information, which was not considered sufficiently crucial to be included in the main body of the paper. Figure A1 presents the dependence of both NAOI and DARF annual values on ONI ones. Linear regression equations are given in the legend of the Figure. Figure A2 provides the annual values of both $netSW_{BOA}$ and $netLW_{BOA}$ under clear skies and in the presence of aerosols in the atmosphere of the Mediterranean region for various ONI events in the period 1980–2022. Linear regression equations are given in the legend of the graph. Figure A3 shows the time evolution of the annual values of DARF and ONI during the period of the study. The purple rectangles indicate a synchronous drop in both ONI and DARF. The values in all three Figures are spatially averaged over the Mediterranean domain selected for the purpose of this work.

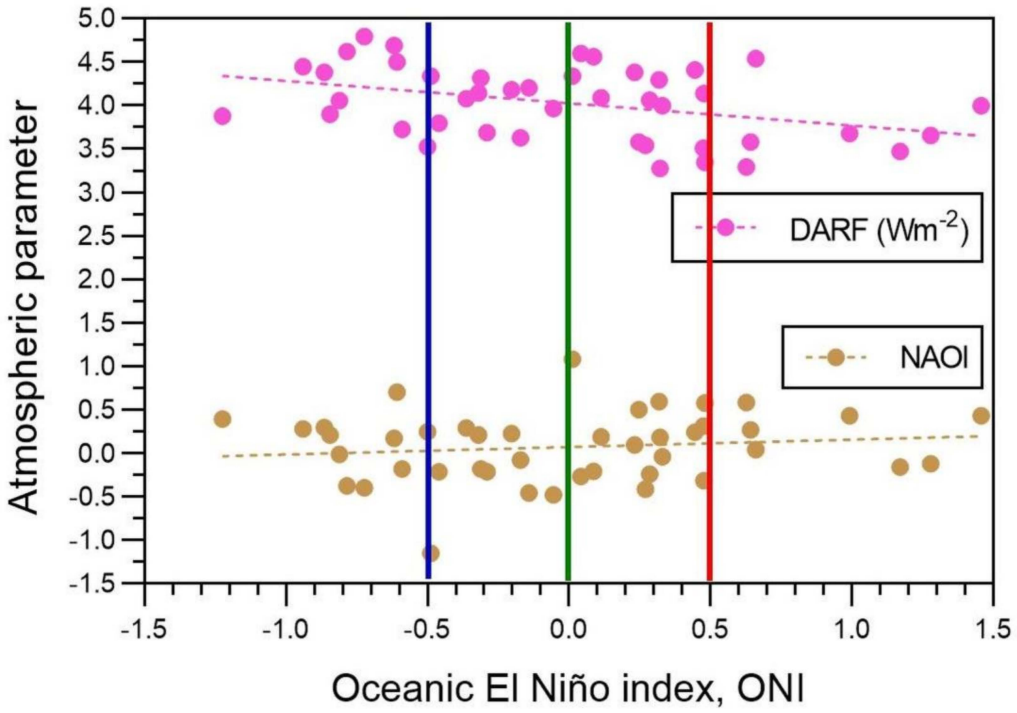



**Figure A1.** Scatter plot of the annual mean (DARF, ONI) and (NAOI, ONI) data pairs over the selected domain of the Mediterranean region in the period 1980–2022. The vertical blue and red solid lines delimit the neutral ENSO events; ONI $\leq -0.5$ denotes negative (cold) La Niña events, and ONI $\geq +0.5$ positive (warm) El Niño ones. The dashed straight lines indicate the linear fits to the two data series with expressions DARF = $-0.2565 \cdot$ONI + 4.0240 with $R^2 = 0.153$, significant at the 95% CI, and NAOI = $+0.0820 \cdot$ONI + 0.0710 with $R^2 = 0.018$, non-significant at the 95% CI.

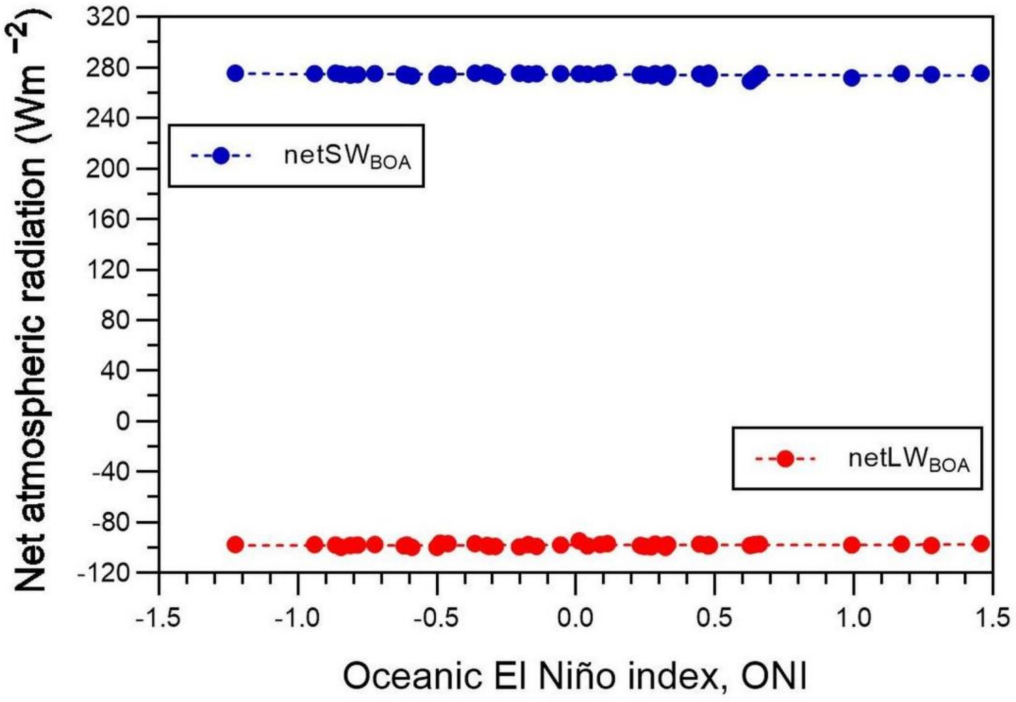



**Figure A2.** Scatter plot of the annual mean ($netSW_{BOA,CS,A}$, ONI) and ($netLW_{BOA,CS,A}$, ONI) data pairs over the selected domain of the Mediterranean region in the period 1980–2022. The vertical blue and red solid lines delimit the neutral ENSO events; ONI $\leq -0.5$ denotes negative (cold) La Niña events, and ONI $\geq +0.5$ positive (warm) El Niño ones. The dashed straight lines indicate the linear fits to the two data series with expressions netSW = $-0.5226 \cdot$ONI + 274.3000 with $R^2 = 0.060$, non-significant at the 95% CI, and netLW = $+0.2354 \cdot$ONI $- 97.9300$ with $R^2 = 0.021$, non-significant at the 95% CI.

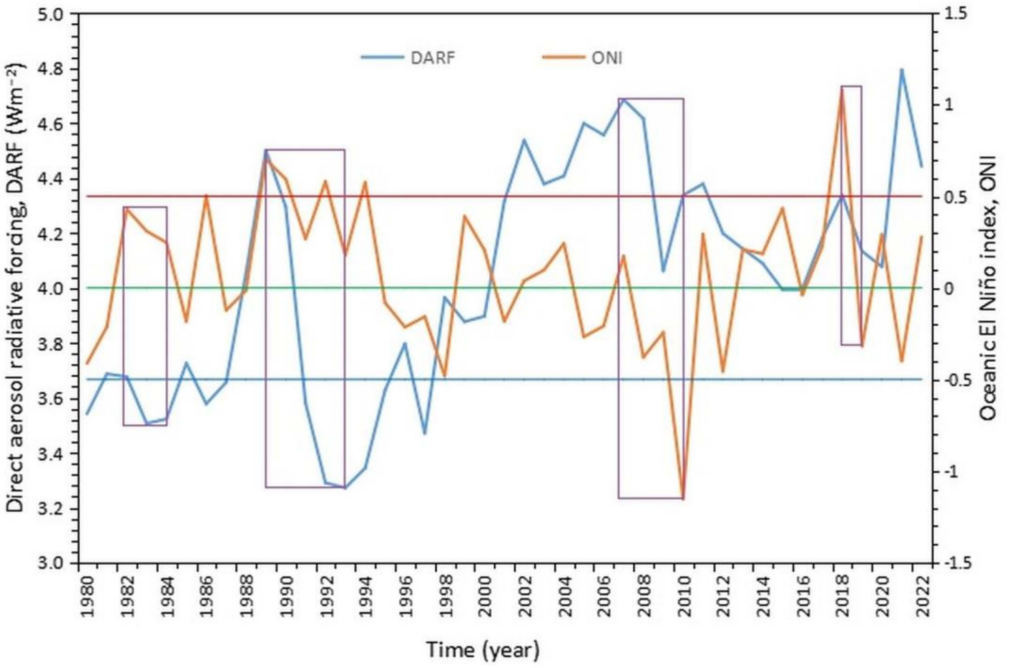



**Figure A3.** Inter-annual variation of DARF and ONI over the selected domain of the Mediterranean region in the period 1980–2022. The horizontal band delimited by ONI = +0.5 (red line) and ONI = $-0.5$ (blue line) refers to neutral ENSO events. Incidences of progressively decreasing positive ENSO occurrences or turning from positive to negative events are shown by vertical purple rectangles; these ONI trends are followed by a synchronous decrease in DARF.

## References


1. Iqbal, M. *An Introduction to Solar Radiation*; Academic Press: New York, NY, USA, 1983.
2. Schulz, M.; Textor, C.; Kinne, S.; Balkanski, Y.; Bauer, S.; Berntsen, T.; Berglen, T.; Boucher, O.; Dentener, F.; Guibert, S.; et al. Radiative Forcing by Aerosols as Derived from the AeroCom Present-Day and Pre-Industrial Simulations. *Atmos. Chem. Phys.* **2006**, *6*, 5225–5246. [CrossRef]
3. Yu, L.; Zhang, M.; Wang, L.; Li, H.; Li, J. Characteristics of Aerosols and Clouds and Their Role in Earth's Energy Budget. *J. Clim.* **2024**, *37*, 995–1014. [CrossRef]
4. Kaskaoutis, D.G.; Kambezidis, H.D.; Adamopoulos, A.D.; Kassomenos, P.A. On the Characterization of Aerosols Using the Ångström Exponent in the Athens Area. *J. Atmos. Sol. Terr. Phys.* **2006**, *68*, 2147–2163. [CrossRef]
5. Chen, Y.; Li, Q.; Kahn, R.A.; Randerson, J.T.; Diner, D.J. Quantifying Aerosol Direct Radiative Effect with Multiangle Imaging Spectroradiometer Observations: Top-of-Atmosphere Albedo Change by Aerosols Based on Land Surface Types. *J. Geophys. Res.* **2009**, *114*, D02109. [CrossRef]
6. Li, J.; Carlson, B.E.; Yung, Y.L.; Lv, D.; Hansen, J.; Penner, J.E.; Liao, H.; Ramaswamy, V.; Kahn, R.A.; Zhang, P.; et al. Scattering and Absorbing Aerosols in the Climate System. *Nat. Rev. Earth Environ.* **2022**, *3*, 363–379. [CrossRef]
7. Martin, R.V.; Jacob, D.J.; Yantosca, R.M.; Chin, M.; Ginoux, P. Global and Regional Decreases in Tropospheric Oxidants from Photochemical Effects of Aerosols. *J. Geophys. Res. Atmos.* **2003**, *108*, 4097. [CrossRef]
8. Kerminen, V.-M. The First Estimates of Global Nucleation Mode Aerosol Concentrations Based on Satellite Measurements. *Atmos. Chem. Phys. Discuss.* **2011**, *11*, 18823–18852. [CrossRef]
9. Sinha, P.R.; Kaskaoutis, D.G.; Manchanda, R.K.; Sreenivasan, S. Characteristics of Aerosols over Hyderabad in Southern Peninsular India: Synergy in the Classification Techniques. *Ann. Geophys.* **2012**, *30*, 1393–1410. [CrossRef]
10. Choobari, O.A.; Zawar-Reza, P.; Sturman, A. The Global Distribution of Mineral Dust and Its Impacts on the Climate System: A Review. *Atmos. Res.* **2014**, *138*, 152–165. [CrossRef]
11. Beegum, S.N.; Gherboudj, I.; Chaouch, N.; Temimi, M.; Ghedira, H. Simulation and Analysis of Synoptic Scale Dust Storms over the Arabian Peninsula. *Atmos. Res.* **2018**, *199*, 62–81. [CrossRef]
12. Ohvril, H.; Teral, H.; Neiman, L.; Kannel, M.; Unstare, M.; Tee, M.; Russak, V.; Okulov, O.; Joëveer, A.; Kallis, A.; et al. Global Dimming and Brightening versus Atmospheric Column Transparency, Europe, 1906–2007. *J. Geophys. Res. Atmos.* **2009**, *114*, 1–17. [CrossRef]
13. Kambezidis, H.D.D.; Founda, D.H.H.; Papanikolaou, N.S.S.; Founda, D.H.H.; Papanikolaou, N.S.S. Linke and Unsworth-Monteith Turbidity Parameters in Athens. *Q. J. R. Meteorol. Soc.* **1993**, *54*, 367–374. [CrossRef]
14. Kambezidis, H.D.; Psiloglou, B.E. Climatology of the Linke and Unsworth-Monteith Turbidity Parameters for Greece: Introduction to the Notion of a Typical Atmospheric Turbidity Year. *Appl. Sci.* **2020**, *10*, 4043. [CrossRef]
15. Babatunde, A.; Vincent, O.O. Estimation of Hourly Clearness Index and Diffuse Fraction Over Coastal and Sahel Regions of Nigeria Using NCEP/NCAR Satellite Data. *J. Energy Res. Rev.* **2021**, *7*, 1–18. [CrossRef]
16. Yang, L.; Cao, Q.; Yu, Y.; Liu, Y. Comparison of Daily Diffuse Radiation Models in Regions of China without Solar Radiation Measurement. *Energy* **2020**, *191*, 116571. [CrossRef]
17. Kambezidis, H.D.; Kampezidou, S.I.; Kampezidou, D. Mathematical Determination of the Upper and Lower Limits of the Diffuse Fraction at Any Site. *Appl. Sci.* **2021**, *11*, 8654. [CrossRef]
18. Yoo, J.M.; Won, Y.I.; Jeong, M.J.; Kim, K.M.; Shin, D.B.; Lee, Y.R.; Cho, Y.J. Intensity of Climate Variability Derived from the Satellite and MERRA Reanalysis Temperatures: AO, ENSO, and QBO. *J. Atmos. Sol. Terr. Phys.* **2013**, *95–96*, 15–27. [CrossRef]
19. Müller, W.A.; Roeckner, E. ENSO Impact on Midlatitude Circulation Patterns in Future Climate Change Projections. *Geophys. Res. Lett.* **2006**, *33*, 1–4. [CrossRef]
20. Abish, B.; Mohanakumar, K. Absorbing Aerosol Variability over the Indian Subcontinent and Its Increasing Dependence on ENSO. *Glob. Planet. Change* **2013**, *106*, 13–19. [CrossRef]
21. Laken, B.A.; Stordal, F. Are There Statistical Links between the Direction of European Weather Systems and ENSO, the Solar Cycle or Stratospheric Aerosols? *R. Soc. Open Sci.* **2016**, *3*, 150320. [CrossRef]
22. Kirov, B.; Georgieva, K. Long-Term Variations and Interrelations of ENSO, NAO and Solar Activity. *Phys. Chem. Earth* **2002**, *27*, 441–448. [CrossRef]
23. Mezzina, B.; García-Serrano, J.; Bladé, I.; Kucharski, F. Dynamics of the ENSO Teleconnection and NAO Variability in the North Atlantic-European Late Winter. *J. Clim.* **2020**, *33*, 907–923. [CrossRef]
24. Casselman, J.W.; Taschetto, A.S.; Domeisen, D.I.V. Nonlinearity in the Pathway of El Ninõ-Southern Oscillation to the Tropical North Atlantic. *J. Clim.* **2021**, *34*, 7277–7296. [CrossRef]
25. Casselman, J.W.; Jiménez-Esteve, B.; Domeisen, D.I.V. Modulation of the El Niño Teleconnection to the North Atlantic by the Tropical North Atlantic during Boreal Spring and Summer. *Weather. Clim. Dyn.* **2022**, *3*, 1077–1096. [CrossRef]
26. García-Serrano, J.; Cassou, C.; Douville, H.; Giannini, A.; Doblas-Reyes, F.J. Revisiting the ENSO Teleconnection to the Tropical North Atlantic. *J. Clim.* **2017**, *30*, 6945–6957. [CrossRef]
27. Liu, Y.; Liu, J.; Xie, M.; Fang, K.; Tarasick, D.W.; Wang, H.; Meng, L.; Cheng, X.; Han, H.; Zhang, X. ENSO Teleconnection to Interannual Variability in Carbon Monoxide Over the North Atlantic European Region in Spring. *Front. Environ. Sci.* **2022**, *10*, 1027. [CrossRef]

28. Alpert, P.; Baldi, M.; Ilani, R.; Krichak, S.; Price, C.; Rodó, X.; Saaroni, H.; Ziv, B.; Kishcha, P.; Barkan, J.; et al. Chapter 2 Relations between Climate Variability in the Mediterranean Region and the Tropics: ENSO, South Asian and African Monsoons, Hurricanes and Saharan Dust. In *Mediterranean*; Lionello, P., Malanotte-Rizzoli, P., Boscolo, R.B.T.-D. in E. and E. S., Eds.; Elsevier: New York, NY, USA, 2006; Volume 4, pp. 149–177. [CrossRef]
29. Mariotti, A.; Zeng, N.; Lau, K.M. Euro-Mediterranean Rainfall and ENSO—A Seasonally Varying Relationship. *Geophys. Res. Lett.* **2002**, *29*, 59-1–59-4. [CrossRef]
30. Mathbout, S.; Lopez-Bustins, J.A.; Royé, D.; Martin-Vide, J.; Benhamrouche, A. Spatiotemporal Variability of Daily Precipitation Concentration and Its Relationship to Teleconnection Patterns over the Mediterranean during 1975–2015. *Int. J. Climatol.* **2020**, *40*, 1435–1455. [CrossRef]
31. Ropelewski, C.F.; Halpert, M.S. Global and Regional Scale Precipitation Patterns Associated with the El Niño/Southern Oscillation. *Mon. Weather. Rev.* **1987**, *115*, 1606–1626. [CrossRef]
32. Urdiales-Flores, D.; Zittis, G.; Hadjinicolaou, P.; Osipov, S.; Klingmüller, K.; Mihalopoulos, N.; Kanakidou, M.; Economou, T.; Lelieveld, J. Drivers of Accelerated Warming in Mediterranean Climate-Type Regions. *NPJ Clim. Atmos. Sci.* **2023**, *6*, 97. [CrossRef]
33. Chiacchio, M.; Wild, M. Influence of NAO and Clouds on Long-Term Seasonal Variations of Surface Solar Radiation in Europe. *J. Geophys. Res. Atmos.* **2010**, *115*, D00D22. [CrossRef]
34. Westervelt, D.M.; Conley, A.J.; Fiore, A.M.; Lamarque, J.F.; Shindell, D.T.; Previdi, M.; Mascioli, N.R.; Faluvegi, G.; Correa, G.; Horowitz, L.W. Connecting Regional Aerosol Emissions Reductions to Local and Remote Precipitation Responses. *Atmos. Chem. Phys.* **2018**, *18*, 12461–12475. [CrossRef]
35. Huang, Y.; Liu, X.; Yin, Z.Y.; An, Z. Global Impact of ENSO on Dust Activities with Emphasis on the Key Region from the Arabian Peninsula to Central Asia. *J. Geophys. Res. Atmos.* **2021**, *126*, e2020JD034068. [CrossRef]
36. Banerjee, P.; Kumar, S.P. ENSO Modulation of Interannual Variability of Dust Aerosols over the Northwest Indian Ocean. *J. Clim.* **2016**, *29*, 1391–1415. [CrossRef]
37. Im, U.; Kanakidou, M. Impacts of East Mediterranean Megacity Emissions on Air Quality. *Atmos. Chem. Phys.* **2012**, *12*, 6335–6355. [CrossRef]
38. Stohl, A.; Aamaas, B.; Amann, M.; Baker, L.H.; Bellouin, N.; Berntsen, T.K.; Boucher, O.; Cherian, R.; Collins, W.; Daskalakis, N.; et al. Evaluating the Climate and Air Quality Impacts of Short-Lived Pollutants. *Atmos. Chem. Phys.* **2015**, *15*, 10529–10566. [CrossRef]
39. Abdelkader, M.; Metzger, S.; Mamouri, R.E.; Astitha, M.; Barrie, L.; Levin, Z.; Lelieveld, J. Dust-Air Pollution Dynamics over the Eastern Mediterranean. *Atmos. Chem. Phys.* **2015**, *15*, 9173–9189. [CrossRef]
40. Kaskaoutis, D.G.; Rashki, A.; Dumka, U.C.; Mofidi, A.; Kambezidis, H.D.; Psiloglou, B.E.; Karagiannis, D.; Petrinoli, K.; Gavriil, A. Atmospheric Dynamics Associated with Exceptionally Dusty Conditions over the Eastern Mediterranean and Greece in March 2018. *Atmos Res* **2019**, *218*, 269–284. [CrossRef]
41. Amiridis, V.; Wandinger, U.; Marinou, E.; Giannakaki, E.; Tsekeri, A.; Basart, S.; Kazadzis, S.; Gkikas, A.; Tayler, M.; Baldasano, J.; et al. Optimizing Saharan Dust CALIPSO Retrievals. *Atmos. Chem. Phys. Discuss.* **2013**, *13*, 14749–14795. [CrossRef]
42. Kaskaoutis, D.G.; Kambezidis, H.D.; Nastos, P.T.; Kosmopoulos, P.G. Study on an Intense Dust Storm over Greece. *Atmos. Environ.* **2008**, *42*, 6884–6896. [CrossRef]
43. Rizza, U.; Barnaba, F.; Marcello Miglietta, M.; Mangia, C.; Di Liberto, L.; Dionisi, D.; Costabile, F.; Grasso, F.; Paolo Gobbi, G. WRF-Chem Model Simulations of a Dust Outbreak over the Central Mediterranean and Comparison with Multi-Sensor Desert Dust Observations. *Atmos. Chem. Phys.* **2017**, *17*, 93–115. [CrossRef]
44. Sicard, M.; Córdoba-Jabonero, C.; Barreto, A.; Welton, E.J.; Gil-Díaz, C.; Carvajal-Pérez, C.V.; Comerón, A.; García, O.; García, R.; López-Cayuela, M.Á.; et al. Volcanic Eruption of Cumbre Vieja, La Palma, Spain: A First Insight to the Particulate Matter Injected in the Troposphere. *Remote Sens.* **2022**, *14*, 2470. [CrossRef]
45. Robock, A.; Matson, M. Circumglobal Transport of the El Chichón Volcanic Dust Cloud. *Science (1979)* **1983**, *221*, 195–197. [CrossRef] [PubMed]
46. Liu, Y.; Kahn, R.A.; Chaloulakou, A.; Koutrakis, P. Analysis of the Impact of the Forest Fires in August 2007 on Air Quality of Athens Using Multi-Sensor Aerosol Remote Sensing Data, Meteorology and Surface Observations. *Atmos Environ.* **2009**, *43*, 3310–3318. [CrossRef]
47. Mishra, A.K.; Klingmueller, K.; Fredj, E.; Lelieveld, J.; Rudich, Y.; Koren, I. Radiative Signature of Absorbing Aerosol over the Eastern Mediterranean Basin. *Atmos. Chem. Phys.* **2014**, *14*, 7213–7231. [CrossRef]
48. Khadgarai, S.; Kumar, V.; Pradhan, P.K. The Connection between Extreme Precipitation Variability over Monsoon Asia and Large-Scale Circulation Patterns. *Atmosphere* **2021**, *12*, 1492. [CrossRef]
49. Yadav, M. South Asian Monsoon Extremes and Climate Change. In *Extremes in Atmospheric Processes and Phenomenon: Assessment, Impacts and Mitigation, Disaster Resilience and Green Growth*; Saxena, P., Shukla, A., Gupta, A.K., Eds.; Springer Nature Singapore Pte Ltd.: Singapore, 2022; pp. 59–86. [CrossRef]
50. Kaskaoutis, D.G.; Kalapureddy, M.C.R.; Devara, P.C.S.; Kosmopoulos, P.G.; Nastos, P.T.; Krishna Moorthy, K.; Kambezidis, H.D. Spatio-Temporal Aerosol Optical Characteristics over the Arabian Sea during the Pre-Monsoon Season. *Atmos. Chem. Phys. Discuss.* **2009**, *9*, 22223–22269. [CrossRef]
51. Casselman, J.W.; Lübbecke, J.F.; Bayr, T.; Huo, W.; Wahl, S.; Domeisen, D.I.V. The Teleconnection of Extreme El Niño-Southern Oscillation (ENSO) Events to the Tropical North Atlantic in Coupled Climate Models. *Weather. Clim. Dyn.* **2023**, *4*, 471–487. [CrossRef]

52. Hochet, A.; Dodet, G.; Ardhuin, F.; Hemer, M.; Young, I. Sea State Decadal Variability in the North Atlantic: A Review. *Climate* **2021**, *9*, 173. [CrossRef]
53. King, M.P.; Keenlyside, N.; Li, C. ENSO Teleconnections in Terms of Non-NAO and NAO Atmospheric Variability. *Clim. Dyn.* **2023**, *61*, 2717–2733. [CrossRef]
54. Casas-Gómez, P.; Sánchez-Salguero, R.; Ribera, P.; Linares, J.C. Contrasting Signals of the Westerly Index and North Atlantic Oscillation over the Drought Sensitivity of Tree-Ring Chronologies from the Mediterranean Basin. *Atmosphere* **2020**, *11*, 644. [CrossRef]
55. Acker, J.G.; Leptoukh, G. Online Analysis Enhances Use of NASA Earth Science Data. *Eos Trans. Am. Geophys. Union.* **2007**, *88*, 14. [CrossRef]
56. Kambezidis, H.D.D. The Solar Resource. In *Comprehensive Renewable Energy*; Elsevier: New York, NY, USA, 2012; Volume 3, pp. 27–84. [CrossRef]
57. Jones, P.D.; Jonsson, T.; Wheeler, D. Extension to the North Atlantic Oscillation Using Early Instrumental Pressure Observations from Gibraltar and South-West Iceland. *Int. J. Climatol.* **1997**, *17*, 1433–1450. [CrossRef]
58. Chen, W.Y.; Van den Dool, H. Sensitivity of Teleconnection Patterns to the Sign of Their Primary Action Center. *Mon. Weather. Rev.* **2003**, *131*, 2885–2899. [CrossRef]
59. Barnston, A.G.; Livezey, R.E. Classification, Seasonality and Persistence of Low-Frequency Atmospheric Circulation Patterns. *Mon. Weather. Rev.* **1987**, *115*, 282. [CrossRef]
60. Compo, G.P.; Whitaker, J.S.; Sardeshmukh, P.D.; Matsui, N.; Allan, R.J.; Yin, X.; Gleason, B.E.; Vose, R.S.; Rutledge, G.; Bessemoulin, P.; et al. The Twentieth Century Reanalysis Project. *Q. J. R. Meteorol. Soc.* **2011**, *137*, 1–28. [CrossRef]
61. Chiu, J.C.; Huang, C.-H.; Marshak, A.; Slutsker, I.; Giles, D.M.; Holben, B.N.; Knyazikhin, Y.; Wiscombe, W.J. Cloud Optical Depth Retrievals from the Aerosol Robotic Network (AERONET) Cloud Mode Observations. *J. Geophys. Res.* **2010**, *115*, D14202. [CrossRef]
62. Min, Q.; Joseph, E.; Duan, M. Retrievals of Thin Cloud Optical Depth from a Multifilter Rotating Shadowband Radiometer. *J. Geophys. Res. Atmos.* **2004**, *109*, 1–10. [CrossRef]
63. Eldering, A.; Kulawik, S.S.; Worden, J.; Bowman, K.; Osterman, G. Implementation of Cloud Retrievals for TES Atmospheric Retrievals: 2. Characterization of Cloud Top Pressure and Effective Optical Depth Retrievals. *J. Geophys. Res. Atmos.* **2008**, *113*, 1–13. [CrossRef]
64. Yu, H.; Kaufman, Y.J.; Chin, M.; Feingold, G.; Remer, L.A.; Anderson, T.L.; Balkanski, Y.; Bellouin, N.; Boucher, O.; Christopher, S.; et al. A Review of Measurement-Based Assessments of the Aerosol Direct Radiative Effect and Forcing. *Atmos. Chem. Phys.* **2006**, *6*, 613–666. [CrossRef]
65. Marinou, E.; Amiridis, V.; Binietoglou, I.; Solomos, S.; Proestakis, E.; Konsta, D.; Tsikerdekis, A.; Papagiannopoulos, N.; Vlastou, G.; Zanis, P.; et al. 3D Evolution of Saharan Dust Transport towards Europe Based on a 9-Year EARLINET-Optimized CALIPSO Dataset. *Atmos. Chem. Phys. Discuss.* **2016**, 1–35. [CrossRef]
66. Kambezidis, H.D. The Solar Radiation Climate of Greece. *Climate* **2021**, *9*, 183. [CrossRef]
67. Mahowald, N.; Albani, S.; Kok, J.F.; Engelstaeder, S.; Scanza, R.; Ward, D.S.; Flanner, M.G. The Size Distribution of Desert Dust Aerosols and Its Impact on the Earth System. *Aeolian Res.* **2014**, *15*, 53–71. [CrossRef]
68. Shaheen, A.; Wu, R.; Yousefi, R.; Wang, F.; Ge, Q.; Kaskaoutis, D.G.; Wang, J.; Alpert, P.; Munawar, I. Spatio-Temporal Changes of Spring-Summer Dust AOD over the Eastern Mediterranean and the Middle East: Reversal of Dust Trends and Associated Meteorological Effects. *Atmos. Res.* **2022**, *281*, 106509. [CrossRef]
69. Ozdemir, E.; Tuna Tuygun, G.; Elbir, T. Application of Aerosol Classification Methods Based on AERONET Version 3 Product over Eastern Mediterranean and Black Sea. *Atmos. Pollut. Res.* **2020**, *11*, 2226–2243. [CrossRef]
70. Chiapello, I.; Formenti, P.; Mbemba Kabuiku, L.; Ducos, F.; Tanré, D.; Dulac, F. Aerosol Optical Properties Derived from POLDER-3/PARASOL (2005–2013) over the Western Mediterranean Sea–Part 2: Spatial Distribution and Temporal Variability. *Atmos. Chem. Phys.* **2021**, *21*, 12715–12737. [CrossRef]
71. Kaskaoutis, D.G.; Kosmopoulos, P.; Kambezidis, H.D.; Nastos, P.T. Aerosol Climatology and Discrimination of Different Types over Athens, Greece, Based on MODIS Data. *Atmos. Environ.* **2007**, *41*, 7315–7329. [CrossRef]
72. Mallet, M.; Dubovik, O.; Nabat, P.; Dulac, F.; Kahn, R.; Sciare, J.; Paronis, D.; Léon, J.F. Absorption Properties of Mediterranean Aerosols Obtained from Multi-Year Ground-Based Remote Sensing Observations. *Atmos. Chem. Phys.* **2013**, *13*, 9195–9210. [CrossRef]
73. Ruckstuhl, C.; Norris, J.R.; Philipona, R. Is There Evidence for an Aerosol Indirect Effect during the Recent Aerosol Optical Depth Decline in Europe? *J. Geophys. Res. Atmos.* **2010**, *115*, 1–7. [CrossRef]
74. Robock, A. Climate Model Simulations of the Effects of the El Chichon Eruption. *Geofis. Int.* **1984**, *23*, 403–414. [CrossRef]
75. Parker, D.E.; Wilson, H.; Jones, P.D.; Christy, J.R.; Folland, C.K. The Impact of Mount Pinatubo on World-Wide Temperatures. *Int. J. Climatol.* **1996**, *16*, 487–497. [CrossRef]
76. Sharafa, S.B.; Aliyu, R.; Ibrahim, B.B.; Tijjani, B.I.; Darma, T.H.; Gana, U.M.; Ayedun, F.; Sulu, H.T. Model Prediction and Climatology of Aerosol Optical Depth (T550) and Angstrom Exponent (A470-660) over Three Aerosol Robotic Network Stations in Sub-Saharan Africa Using Moderate Resolution Imaging Spectroradiometer Data. *Niger. J. Technol.* **2020**, *39*, 255–268. [CrossRef]
77. Serrano, D.; Marín, M.J.; Núñez, M.; Utrillas, M.P.; Gandía, S.; Martínez-Lozano, J.A. Wavelength Dependence of the Effective Cloud Optical Depth. *J. Atmos. Sol. Terr. Phys.* **2015**, *130–131*, 14–22. [CrossRef]
78. Luccini, E.; Rivas, M.; Rojas, E. Cloud Optical Depth from Total and UV Solar Irradiance Measurements at Two Sites of the Atacama Desert in Chile. *Atmos. Res.* **2016**, *174–175*, 18–30. [CrossRef]
79. Mörner, N.-A. The Approaching New Grand Solar Minimum and Little Ice Age Climate Conditions. *Nat. Sci.* **2015**, *7*, 510–518. [CrossRef]

80. Korras-Carraca, M.B.; Gkikas, A.; Matsoukas, C.; Hatzianastassiou, N. Global Clear-Sky Aerosol Speciated Direct Radiative Effects over 40 Years (1980–2019). *Atmosphere* **2021**, *12*, 1254. [CrossRef]
81. Kambezidis, H.D.; Kambezidou, D.H. The Solar Dimming Effect over the Mediterranean Region. In Proceedings of the 5th International Conference SOLARIS, Brno, Czech Republic, 10–11 August 2011; pp. 116–121.
82. Kambezidis, H.D.; Kaskaoutis, D.G.; Kalliampakos, G.K.; Rashki, A.; Wild, M. The Solar Dimming/Brightening Effect over the Mediterranean Basin in the Period 1979–2012. *J. Atmos. Sol. Terr. Phys.* **2016**, *150–151*, 31–46. [CrossRef]
83. Papadimas, C.D.; Hatzianastassiou, N.; Matsoukas, C.; Kanakidou, M.; Mihalopoulos, N.; Vardavas, I. The Direct Effect of Aerosols on Solar Radiation over the Broader Mediterranean Basin. *Atmos. Chem. Phys.* **2012**, *12*, 7165–7185. [CrossRef]
84. Gao, P.X. Long-Term Trend of Sunspot Numbers. *Astrophys. J.* **2016**, *830*, 140. [CrossRef]
85. Veronig, A.M.; Jain, S.; Podladchikova, T.; Pötzi, W.; Clette, F. Hemispheric Sunspot Numbers 1874–2020. *Astron. Astrophys.* **2021**, *652*, A56. [CrossRef]
86. Nastos, P.T.; Kambezidis, H.D.; Demetriou, D. Solar Dimming/Brightening within the Mediterranean. In Proceedings of the 13th International Conference on Environmental Science and Technology, Athens, Greece, 5–7 September 2013; Volume 12.
87. Sanchez-Lorenzo, A.; Calbó, J.; Brunetti, M.; Deser, C. Dimming/Brightening over the Iberian Peninsula: Trends in Sunshine Duration and Cloud Cover and Their Relations with Atmospheric Circulation. *J. Geophys. Res. Atmos.* **2009**, *114*, D00D09. [CrossRef]
88. Wild, M.; Trüssel, B.; Ohmura, A.; Long, C.N.; König-Langlo, G.; Dutton, E.G.; Tsvetkov, A. Global Dimming and Brightening: An Update beyond 2000. *J. Geophys. Res. Atmos.* **2009**, *114*, 1–14. [CrossRef]
89. Stamatis, M.; Hatzianastassiou, N.; Korras-Carraca, M.B.; Matsoukas, C.; Wild, M.; Vardavas, I. An Assessment of Global Dimming and Brightening during 1984-2018 Using the FORTH Radiative Transfer Model and ISCCP Satellite and MERRA-2 Reanalysis Data. *Atmosphere* **2023**, *14*, 1258. [CrossRef]
90. Ioannidis, E.; Lolis, C.J.; Papadimas, C.D.; Hatzianastassiou, N.; Bartzokas, A. On the Intra-Annual Variation of Cloudiness over the Mediterranean Region. *Atmos. Res.* **2018**, *208*, 246–256. [CrossRef]
91. Pastor, F.; Valiente, J.A.; Khodayar, S. A Warming Mediterranean: 38 Years of Increasing Sea Surface Temperature. *Remote Sens.* **2020**, *12*, 2687. [CrossRef]
92. Katsoulis, B.; Kambezidis, H. Variation of Cloudiness and Sunshine in the Greek Mainland. *Z. Für Meteorol.* **1987**, *37*, 278–284.
93. Founda, D.; Nastos, P.T.; Pierros, F.; Kalimeris, A. Historical Observations of Cloudiness (1882–2012) over a Large Urban Area of the Eastern Mediterranean (Athens). *Theor. Appl. Clim.* **2019**, *137*, 283–295. [CrossRef]
94. Norris, J.R.; Wild, M. Trends in Aerosol Radiative Effects over Europe Inferred from Observed Cloud Cover, Solar "Dimming", and Solar "Brightening". *J. Geophys. Res. Atmos.* **2007**, *112*, 1–13. [CrossRef]
95. Raptis, I.-P.P.; Kazadzis, S.; Amiridis, V.; Gkikas, A.; Gerasopoulos, E.; Mihalopoulos, N. A Decade of Aerosol Optical Properties Measurements over Athens, Greece. *Atmosphere* **2020**, *11*, 154. [CrossRef]
96. Nabat, P.; Somot, S.; Mallet, M.; Sanchez-Lorenzo, A.; Wild, M. Contribution of Anthropogenic Sulfate Aerosols to the Changing Euro-Mediterranean Climate since 1980. *Geophys. Res. Lett.* **2014**, *41*, 5605–5611. [CrossRef]
97. Samman, A.E.; Butt, M.J. Aerosol Types and Their Climatology over the Dust Belt Region. *Atmosphere* **2023**, *14*, 1610. [CrossRef]
98. Pace, G.; di Sarra, A.; Meloni, D.; Piacentino, S.; Chamard, P. Aerosol Optical Properties at Lampedusa (Central Mediterranean). 1. Influence of Transport and Identification of Different Aerosol Types. *Atmos. Chem. Phys.* **2006**, *6*, 697–713. [CrossRef]
99. Kaufman, Y.J. Biomass Burning Airborne and Spaceborne Experiment in the Amazonas (BASE-A). *J. Geophys. Res.* **1992**, *97*, 14581–14599. [CrossRef]
100. Holben, B.N.; Eck, T.F.; Fraser, R.S. Temporal and Spatial Variability of Aerosol Optical Depth in the Sahel Region in Relation to Vegetation Remote Sensing. *Int. J. Remote Sens.* **1991**, *12*, 1147–1163. [CrossRef]
101. Filonchyk, M.; Hurynovich, V.; Yan, H. Trends in Aerosol Optical Properties over Eastern Europe Based on MODIS-Aqua. *Geosci. Front.* **2020**, *11*, 2169–2181. [CrossRef]
102. Kaskaoutis, D.G.G.; Kharol, S.K.K.; Sinha, P.R.R.; Singh, R.P.P.; Kambezidis, H.D.D.; Rani Sharma, A.; Badarinath, K.V.S.V.S. Extremely Large Anthropogenic-Aerosol Contribution to Total Aerosol Load over the Bay of Bengal during Winter Season. *Atmos. Chem. Phys.* **2011**, *11*, 7097–7117. [CrossRef]
103. Damiano, R.; Sannino, A.; Amoruso, S.; Boselli, A. Aerosol Characterization with Long-Term AERONET Sun-Photometer Measurements in the Naples Mediterranean Area. *Atmosphere* **2022**, *13*, 2078. [CrossRef]
104. Kalapureddy, M.C.R.; Kaskaoutis, D.G.; Ernest Raj, P.; Devara, P.C.S.; Kambezidis, H.D.; Kosmopoulos, P.G.; Nastos, P.T. Identification of Aerosol Type over the Arabian Sea in the Premonsoon Season during the Integrated Campaign for Aerosols, Gases and Radiation Budget (ICARB). *J. Geophys. Res. Atmos.* **2009**, *114*, D17203. [CrossRef]
105. Kalapureddy, M.C.R.; Devara, P.C.S. Characterization of Aerosols over Oceanic Regions around India during Pre-Monsoon 2006. *Atmos Environ.* **2008**, *42*, 6816–6827. [CrossRef]
106. Al-taie, K.B.; Rajab, J.M.; Al-salihi, A.M. Climatology and Classification of Aerosols Based on Optical Properties over Selected Stations in Iraq. In Proceedings of the 8th International Conference on Applied Science and Technology (ICAST 2020), Bahir Dar, Ethiopia, 2–4 October 2020; Volume 050041, pp. 1–12.
107. Logothetis, S.A.; Salamalikis, V.; Kazantzidis, A. Aerosol Classification in Europe, Middle East, North Africa and Arabian Peninsula Based on AERONET Version 3. *Atmos. Res.* **2020**, *239*, 104893. [CrossRef]

108. Szkop, A.; Pietruczuk, A.; Posyniak, M. Classification of Aerosol over Central Europe by Cluster Analysis of Aerosol Columnar Optical Properties & Backward Trajectory Statistics. *Acta Geophys.* **2016**, *64*, 2650–2676.
109. Gharibzadeh, M.; Alam, K.; Abedini, Y.; Bidokhti, A.A. Classification of Aerosols Using Multiple Clustering Techniques over Zanjan, Iran, during 2010–2014. In Proceedings of the E3S Web of Conferences, Dushanbe, Tajikistan, 8–12 April 2019; Volume 99, pp. 1–5. [CrossRef]
110. Kaskaoutis, D.G.; Kambezidis, H.D.; Hatzianastassiou, N.; Kosmopoulos, P.G.; Badarinath, K.V.S. Aerosol Climatology: On the Discrimination of Aerosol Types over Four AERONET Sites. *Atmos. Chem. Phys. Discuss.* **2007**, *7*, 6357–6411. [CrossRef]
111. Gerasopoulos, E.; Amiridis, V.; Kazadzis, S.; Kokkalis, P.; Eleftheratos, K.; Andreae, M.O.; Andreae, T.W.; El-Askary, H.; Zerefos, C.S. Three-Year Ground Based Measurements of Aerosol Optical Depth over the Eastern Mediterranean: The Urban Environment of Athens. *Atmos. Chem. Phys.* **2011**, *11*, 2145–2159. [CrossRef]
112. Bruley, E.; Mouillot, F.; Lauvaux, T.; Rambal, S. Enhanced Spring Warming in a Mediterranean Mountain by Atmospheric Circulation. *Sci. Rep.* **2022**, *12*, 7721. [CrossRef]
113. Aurelle, D.; Thomas, S.; Albert, C.; Bally, M.; Bondeau, A.; Boudouresque, C.; Cahill, A.E.; Carlotti, F.; Chenuil, A.; Cramer, W.; et al. Biodiversity, Climate Change, and Adaptation in the Mediterranean. *Ecosphere* **2022**, *13*, e3915. [CrossRef]


**Disclaimer/Publisher's Note:** The statements, opinions and data contained in all publications are solely those of the individual author(s) and contributor(s) and not of MDPI and/or the editor(s). MDPI and/or the editor(s) disclaim responsibility for any injury to people or property resulting from any ideas, methods, instructions or products referred to in the content.